

ORIGINAL ARTICLE

Layer 6A Pyramidal Cell Subtypes Form Synaptic Microcircuits with Distinct Functional and Structural Properties

Danqing Yang^{1,†}, Guanxiao Qi^{1,†}, Chao Ding¹ and Dirk Feldmeyer^{1,2,3}

¹Research Center Juelich, Institute of Neuroscience and Medicine 10, 52425 Juelich, Germany, ²RWTH Aachen University Hospital, Dept of Psychiatry, Psychotherapy, and Psychosomatics, 52074 Aachen, Germany and ³Jülich-Aachen Research Alliance, Translational Brain Medicine (JARA Brain), Aachen, Germany

Address correspondence to Dirk Feldmeyer, Research Center Juelich, Institute of Neuroscience and Medicine 10, Section 'Function of Neuronal Microcircuits', Leo-Brandt-Strasse, Juelich 52425, Germany. Email: d.feldmeyer@fz-juelich.de

[†]The authors Danqing Yang and Guanxiao Qi have contributed equally to this work

Abstract

Neocortical layer 6 plays a crucial role in sensorimotor co-ordination and integration through functionally segregated circuits linking intracortical and subcortical areas. We performed whole-cell recordings combined with morphological reconstructions to identify morpho-electric types of layer 6A pyramidal cells (PCs) in rat barrel cortex. Cortico-thalamic (CT), cortico-cortical (CC), and cortico-claustral (CCLa) PCs were classified based on their distinct morphologies and have been shown to exhibit different electrophysiological properties. We demonstrate that these three types of layer 6A PCs innervate neighboring excitatory neurons with distinct synaptic properties: CT PCs establish weak facilitating synapses onto other L6A PCs; CC PCs form synapses of moderate efficacy, while synapses made by putative CCLa PCs display the highest release probability and a marked short-term depression. For excitatory-inhibitory synaptic connections in layer 6, both the presynaptic PC type and the postsynaptic interneuron type govern the dynamic properties of the respective synaptic connections. We have identified a functional division of local layer 6A excitatory microcircuits which may be responsible for the differential temporal engagement of layer 6 feed-forward and feedback networks. Our results provide a basis for further investigations on the long-range CC, CT, and CCLa pathways.

Key words: barrel cortex, cortico-claustral, cortico-cortical, cortico-thalamic, layer 6A

Introduction

Early born excitatory neurons in the ventricular zone migrate into the cortical plate to occupy deep layers; layer 6 (L6) is the first neocortical layer to form (Rakic 2009; Lodato and Arlotta 2015). In rat barrel cortex, layer 6 is the thickest layer and contains the highest number of neurons (Hutsler et al. 2005; Meyer et al. 2010). Pyramidal cells (PCs) in layer 6 of the neocortex display a high degree of morphological, electrophysiological, and molecular diversity (Zhang and Deschenes 1997; Kumar and Ohana 2008; Thomson 2010; Marx and Feldmeyer

2013; Gouwens et al. 2019; Kast et al. 2019; Egger et al. 2020; Gouwens et al. 2020). They project either “intratelencephalically” (IT) within the cortex, to the striatum, and the claustrum or “extratelencephalically” (ET) to, for example, different thalamic nuclei (for a review, see Rockland 2019). This heterogeneity makes it difficult to elucidate the exact functional and structural properties of the L6A synaptic microcircuitry. Compared with PCs in other neocortical layers, L6 PCs have been found to rarely establish intralaminar synaptic contacts, and if so, they generally display a low synaptic release probability (Beierlein and

Connors 2002; Mercer et al. 2005; West et al. 2006; Crandall et al. 2017; Seeman et al. 2018). Hence, a systematic and comprehensive study of excitatory synaptic microcircuits in layer 6 is still missing.

As the pre-eminent source of cortico-thalamic (CT) projections, L6 microcircuits provide contextual modulation in the feedback loop of the sensory processing system (Harris and Mrcsic-Flogel 2013; Velez-Fort et al. 2014). The two major types of L6A principal cells, the ET CT PCs and the IT cortico-cortical (CC) PCs, show distinct axonal projection patterns and participate in distinct microcircuits within the neocortical network (Kumar and Ohana 2008; Pichon et al. 2012; Sundberg et al. 2018). CT PCs are known to generate weak and facilitatory excitatory postsynaptic responses onto both excitatory and inhibitory neurons (West et al. 2006; Frandolig et al. 2019). Conversely, L6A CC PCs have been proposed to innervate L6A PCs and parvalbumin (PV)-positive interneurons; these synapses exhibit short-term synaptic depression (Mercer et al. 2005; Yang et al. 2020). Apart from L6A CC PCs, there is another class of IT L6A PCs that shows axonal projections predominantly to the ipsilateral claustrum (cortico-claustral [CCLa] PCs). The claustrum itself is reciprocally connected with most neocortical areas and targets all cortical laminae, although connections with sensory cortices are generally weaker than those with more frontal cortical regions (Zakiewicz et al. 2014; Atlan et al. 2017; Zingg et al. 2018; Rockland 2019; Gouwens et al. 2020). Among other functions, such as the regulation of attention, the claustrum is considered to co-ordinate sensory and motor modalities from different cortical areas (Bayat et al. 2018; for a review, see Naghavi et al. 2007; Smith et al. 2017; Zingg et al. 2018; Jackson et al. 2020). In humans, the claustrum together with the striatum (also a part of the telencephalon) has been proposed to participate in a salience network which is known to integrate sensory, emotional, and cognitive information (Peters et al. 2016; Smith, Watson, et al. 2019).

Therefore, it is important to study the role of IT PCs in driving specific intracortical networks and in conveying sub-cortical output. To systematically investigate the L6A excitatory microcircuitry, we performed patch-clamp recordings and morphological reconstructions. In contrast to most other studies focusing only on corticocortical and corticothalamic neurons, we demonstrated that another IT PC subtype (putative CCLa PC) is also present in rat barrel cortex and displays distinct morphological, electrophysiological, and in particular, synaptic properties. CT, CC, and putative CCLa PCs were clearly classified based on their morphological properties. This subdivision is supported by the fact that these three PC subtypes also exhibit distinct electrophysiological properties. Using paired recordings from synaptically coupled neurons, we found that different PC types establish synapses with other L6A excitatory neurons that show very distinct properties. More specifically, L6A CT PCs form synapses with other L6A PCs that have a low release probability and exhibit a short-term facilitation. Synapses made by presynaptic CC PCs are generally stronger, and those established by putative CCLa PCs display the highest release probability and a marked short-term depression. Moreover, we demonstrate here that, for excitatory-inhibitory synaptic connections, both the presynaptic PC type and the postsynaptic interneuron type govern the properties of synaptic release. Our results reveal a neuronal cell type-specific and functionally distinct organization of L6A excitatory microcircuits in the rat barrel cortex.

Materials and Methods

Slice Preparation

All experimental procedures involving animals were performed in accordance with the guidelines of the Federation of European Laboratory Animal Science Association, the EU Directive 2010/63/EU, and the German animal welfare law. In this study, Wistar rats (Charles River, either sex) aged 17–21 postnatal days were anesthetized with isoflurane and decapitated. The brain was quickly removed and placed in an ice-cold artificial cerebrospinal fluid (ACSF) containing a high Mg^{2+} and a low Ca^{2+} concentration (4 mM $MgCl_2$ and 1 mM $CaCl_2$) to reduce potentially excitotoxic synaptic transmission during slicing. In order to maintain adequate oxygenation and a physiological pH level, the solution was constantly bubbled with carbogen gas (95% O_2 and 5% CO_2). The brain was then placed on the ramp of a slope of 10° and was cut at an angle of 50° to the midline (Agmon and Connors 1991). Thalamocortical slices were cut at 350 μm thickness using a high-vibration frequency and were then transferred to an incubation chamber for a recovery period of 30–60 min at room temperature.

During whole-cell patch-clamp recordings, slices were continuously superfused (perfusion speed ~ 5 ml/min) with ACSF containing (in mM): 125 NaCl, 2.5 KCl, 1.25 NaH_2PO_4 , 1 $MgCl_2$, 2 $CaCl_2$, 25 $NaHCO_3$, 25 D-glucose, 3 mho-inositol, 2 sodium pyruvate, and 0.4 ascorbic acid, bubbled with carbogen gas and maintained at 30–33 $^\circ C$. Patch pipettes were pulled from thick-wall borosilicate glass capillaries and filled with an internal solution containing (in mM): 135 K-gluconate, 4 KCl, 10 HEPES, 10 phosphocreatine, 4 Mg-ATP, and 0.3 GTP (pH 7.4 with KOH, 290–300 mOsm). The “searching” pipette (see below) was filled with an internal solution in which K^+ is replaced by Na^+ (containing [in mM]: 105 Na-gluconate, 30 NaCl, 10 HEPES, 10 phosphocreatine, 4 Mg-ATP, and 0.3 GTP) in order to prevent the depolarization of neurons during searching for a presynaptic cell. Biocytin was added to the internal solution at a concentration of 3–5 mg/ml in order to stain patched neurons; a recording time >15 min was necessary for an adequate diffusion of biocytin into dendrites and axons of targeted cells (Marx et al. 2012). No biocytin was added to the Na-based internal solution for “searching” pipettes.

Electrophysiological Recordings

Neurons were visualized using infrared differential interference contrast microscopy. Barrels in the primary somatosensory cortex can be identified in layer 4 as dark stripes with light “hollows” and were visible in six to eight consecutive slices (Agmon and Connors 1991; Feldmeyer et al. 1999). In the acute slice, the difference in soma size marks the difference between L5 and L6 pyramidal neurons. L6A neurons were recorded in the upper 65% of layer 6, while neurons in the L6B lower 35% (Woo et al. 1991; Clancy and Cauler 1999; Marx and Feldmeyer 2013) were not used for recordings. In general, L6A neurons were recorded from 480 to 900 μm below the layer 4–layer 5A border. Putative PCs and interneurons were differentiated on the basis of their intrinsic action potential (AP) firing pattern during recording and after post hoc histological staining also by their morphological appearance.

Whole-cell patch clamp recordings were made using an EPC10 amplifier (HEKA). Signals were sampled at 10 kHz, filtered at 2.9 kHz using Patchmaster software (HEKA), and

later analyzed off-line using Igor Pro software (Wavemetrics). Recordings were performed using patch pipettes of resistance between 6 and 10 M Ω . Because the intralaminar connectivity ratio in L6A is low, we performed a “searching procedure” described previously after patching a potential postsynaptic neuron (Feldmeyer et al. 1999; Feldmeyer and Radnikow 2016). “Searching” pipettes (see above) were used to identify synaptic connections: When an AP elicited in “loose cell-attached” mode resulted in an excitatory postsynaptic potential (EPSP) in the postsynaptic neuron, this presynaptic neuron was repatched with a new pipette filled with biocytin-containing internal solution.

Histological Staining

After single-cell or paired recordings, brain slices containing biocytin-filled neurons were fixed for at least 24 h at 4 °C in 100 mM phosphate buffer solution (PBS, pH 7.4) containing 4% paraformaldehyde (PFA). After rinsing slices several times in 100 mM PBS, they were treated with 1% H₂O₂ in PBS for about 20 min in order to reduce any endogenous peroxidase activity. Slices were rinsed repeatedly with PBS and then incubated in 1% avidin-biotinylated horseradish peroxidase (Vector ABC staining kit, Vector Lab. Inc.) containing 0.1% Triton X-100 for 1 h at room temperature. The reaction was catalyzed using 0.5 mg/mL 3,3'-diaminobenzidine (DAB; Sigma-Aldrich) as a chromogen. Slices were then rinsed with 100 mM PBS, followed by slow dehydration with ethanol in increasing concentrations, and finally in xylene for 2–4 h. After that, slices were embedded using Eukitt medium (Otto Kindler GmbH).

In a subset of experiments, we tried to identify the expression of the molecular marker forkhead box protein P2 (FoxP2) in L6A PCs recorded in acute brain slices to investigate a possible correlation with the electrophysiological and morphological properties. To this end, during electrophysiological recordings, Alexa Fluor 594 dye (1:500, Invitrogen) was added to the internal solution for post hoc identification of patched neurons. After recording, slices (350 μ m) were fixed with 4% PFA in 100 mM PBS for at least 24 h at 4 °C and then permeabilized in 1% milk powder solution containing 0.5% Triton X-100 and 100 mM PBS. Primary and secondary antibodies were diluted in the permeabilization solution (0.5% Triton X-100 and 100 mM PBS) shortly before the antibody incubation. For single-cell FoxP2 staining, slices were incubated overnight with Goat-anti-FoxP2 primary antibody (1:500, Santa Cruz Biotechnology) at 4 °C and then rinsed thoroughly with 100 mM PBS. Subsequently, slices were treated with Alexa Fluor secondary antibodies (1:500) for 2–3 h at room temperature in the dark. After rinsing with 100 mM PBS, the slices were embedded in Fluoromount. Fluorescence images were taken using the Olympus CellSens platform. The position of the patched neurons was identified by the biocytin-conjugated Alexa dye so that the expression of FoxP2 could be tested in biocytin-stained neurons. After acquiring fluorescent images, slices were incubated in 100 mM PBS overnight and then used for subsequent histological processing as described above.

Morphological 3D Reconstructions

Computer-assisted morphological 3D reconstructions of biocytin-filled L6A neurons were made using NEUROLUCIDA[®] software (MicroBrightField) and Olympus B61 microscopy at 1000 \times magnification (100 \times objective and 10 \times eyepiece). Neurons were selected for reconstruction based on the quality of biocytin labelling when background staining was minimal. The cell

body and dendritic and axonal branches were reconstructed manually under constant visual inspection to detect thin and small collaterals. Barrel and layer borders, pial surface, and white matter were delineated during reconstructions at a lower magnification. The position of soma and layers were confirmed by superimposing the differential interference contrast images taken during the recording. The tissue shrinkage was corrected using correction factors of 1.1 in the x–y direction and 2.1 in the z direction (Marx et al. 2012). Analysis of 3D-reconstructed neurons was done with NEUROEXPLORER[®] software (MicroBrightField). Putative synaptic contacts were identified as close appositions of presynaptic axon terminals and postsynaptic dendrites in the same focal plane under light microscopy with 100 \times objective and 10 \times eyepiece. The distance between the soma and a putative synaptic contact was calculated as the path length along the dendrite from the location of synaptic contact to soma in 3D space.

Unsupervised Hierarchical Cluster Analysis

Eight morphological parameters were used for unsupervised cluster analysis. Parameters were standardized using z-score in order to make the distributions numerically comparable. Principal component analysis (PCA) was used to analyze the interdependence between variables and to reduce the dimensionality of the dataset while preserving maximum variability. PCA reduces the redundancy of the dataset by eliminating correlated variables and produces linear combinations of the original variables to generate new axes. To determine the number of principal components to retain for cluster analysis, we used Kaiser's rule, an objective way to determine the number of clusters by leaving all components with eigenvalues <1. Since the dataset is standardized, the variables have an eigenvalue of 1, and hence, PCs with an eigenvalue >1 describe more of the data's variance than the original variable.

Classification of PC subtypes was then performed using unsupervised hierarchical cluster analysis employing Ward's method (Ward 1963). This method utilizes a minimum variance criterion to combine cells into clusters at each stage, which minimizes the total within-cluster variance. Euclidean distance was used to calculate the variance. A dendrogram was constructed to visualize the distance at which clusters are combined.

Density Maps

The 3D density maps of axonal and dendritic length were obtained using computerized 3D reconstructions, where the length of the axonal and dendritic tree per unit volume of 50 \times 50 \times 50 μ m³ was calculated. The soma center of each neuron in a single cluster was aligned and given the co-ordinates of X, Y, and Z=(0, 0, 0). The relative co-ordinate of the beginning and the endpoint of each segment in the tracing were obtained using the segment point analysis in NEUROEXPLORER. Further steps were carried out in Matlab (MathWorks) using a custom-written algorithm (courtesy of Drs G. Qi and H. Wang). The 3D axonal and dendritic density maps were calculated for each reconstructed neuron in this cluster and were then averaged to obtain the 3D density map. The averaged curve of single group was made by aligning the soma position of individual profile and was smoothed using the 3D smooth function in Matlab with a Gaussian kernel (standard deviation (SD) = 50 μ m). Isosurfaces at the 80 percentile were calculated for the smoothed density maps. Finally, dendritic and axonal density

maps were visualized after projecting to 2D or 1D using two different colors, red and blue, respectively.

Electrophysiological Analysis

Custom-written macros for Igor Pro 6 (WaveMetrics) were used to analyze the recorded electrophysiological signals. Neurons with a series resistance $>45\text{ M}\Omega$ ($50\text{ M}\Omega$ for neurons from paired recordings, series resistance was compensated by 80%) or with a depolarized membrane potential ($>-50\text{ mV}$) after rupturing the cell membrane were excluded from data analysis. Passive and active AP properties were assessed by eliciting a series of initially hyperpolarizing, followed by depolarizing 1-s current pulses under current clamp configuration. The resting membrane potential of the neuron was measured directly after breakthrough into the whole-cell configuration with no current injection. To calculate the input resistance, the slope of the linear fit to the voltage step from -60 to -70 mV of the current–voltage relationship was used (Ziegler et al. 2010). The rheobase current was defined as the minimal current that elicited the first spike. The spike threshold was defined as the point of maximal acceleration of the membrane potential using the second derivative (d^2V/dt^2), that is, the time point with the fastest voltage change. The spike amplitude was calculated as the difference in voltage from AP threshold to the peak during depolarization. The spike half-width (HW) was measured as the time difference between rising phase and decaying phase of the spike at half-maximum amplitude. Interspike interval (ISI) was measured as the average time taken between individual spikes at the current step that elicited close to 10 APs. The adaptation ratio was measured as the ratio of the 10th ISI and the 2nd ISI.

Synaptic properties were evaluated as described previously (Feldmeyer et al. 1999; Feldmeyer et al. 2002). All uEPSP recordings were aligned to their corresponding presynaptic AP peaks, and an average sweep was generated as the mean uEPSP. The EPSP amplitude was calculated as the difference between the mean baseline and maximum voltage of the postsynaptic event. The paired-pulse ratio was defined as the second/third uEPSP divided by the first uEPSP amplitude elicited by presynaptic APs at a stimulation frequency of 10 Hz. Failures were defined as events with an amplitude $<1.5\times$ the SD of the noise within the baseline window; the failure rate refers to the percentage of failures. The coefficient of variation (CV) was calculated as the SD divided by the mean uEPSP amplitude. Rise time was calculated as the mean time to rise from 20% to 80% of the peak amplitude. The latency was calculated as the time interval between the peak amplitude of presynaptic AP and the onset of the EPSP. The decay time was measured using a single exponential fit to the decay phase of both individual and averaged responses. The properties mentioned above were obtained from 20 to 80 successive sweeps.

Statistics

Data were either presented as box plots ($n > 10$) or as bar histograms ($n < 10$). For box plots, the interquartile range (IQR) is shown as a box, the range of values that are within $1.5\times$ IQR are shown as whiskers and the median is represented by a horizontal line in the box; for bar histograms, the mean \pm SD are given. Statistical comparisons between multiple groups were done using a Kruskal–Wallis test followed by a post hoc Wilcoxon Mann–Whitney U test between individual groups. Wilcoxon Mann–Whitney U test was performed to access the significant difference between individual clusters. Statistical significance was

set at $P < 0.05$, and n indicates the number of neurons/pairs analyzed.

Results

Three Types of Morphologically and Electrophysiologically Distinct L6A PCs in Rat Barrel Cortex

Whole-cell recordings from L6A excitatory neurons with simultaneous biocytin fillings were performed in acute brain slices of rat barrel cortex allowing post hoc identification of their morphologies. Layer 6B was identified as a small dark band of approximately $200\text{ }\mu\text{m}$ width that is located between layer 6A and the white matter (Marx and Feldmeyer 2013). As a remnant of the subplate layer of the cerebral cortex, layer 6B has a specific molecular marker expression and contains a heterogeneous population of the earliest-generated excitatory neurons with atypical morphologies (Hoerder-Suabedissen et al. 2009; Oeschger et al. 2012; Hoerder-Suabedissen et al. 2013; Marx et al. 2017). In this study, neurons in layer 6B were excluded from the analysis. Neurons with incomplete filling, high background staining, or major truncations of the dendrites were excluded from the morphological analysis, resulting in 41 high-quality 3D reconstructions of L6A PCs (Supplementary Fig. S1). In order to objectively classify L6A pyramidal neurons, a hierarchical cluster analysis was performed basing on their morphological properties. Three clusters of L6A PCs can be clearly identified by distinct dendritic and axonal projecting patterns (Fig. 1A–C). In accordance with previous studies, we refer to these clusters of L6 pyramidal neurons as CT, CC, and CClA PCs on the basis of their morphological features (Katz 1987; Kumar and Ohana 2008; Baker et al. 2018; Cotel et al. 2018). CT-like PCs (cluster 1) have an apical dendrite terminating predominately in layer 4 and axonal collaterals that project vertically. Their basal dendrites and axons are comparatively short ($1899 \pm 447\text{ }\mu\text{m}$ for length of basal dendrites and $5502 \pm 2189\text{ }\mu\text{m}$ for axonal length, respectively) and have a small horizontal fieldspan ($231 \pm 58\text{ }\mu\text{m}$ for dendritic and $529 \pm 240\text{ }\mu\text{m}$ for axonal horizontal fieldspan, respectively). Dendrites of upright CC PCs (cluster 2) resemble those of CT PCs. Their apical dendrites project toward the pial surface and terminate in layer 4 or layer 5A. Basal dendrites, however, are longer than those of CT PCs and have a larger horizontal fieldspan (length: $3684 \pm 1286\text{ }\mu\text{m}$; horizontal dendritic fieldspan: $394 \pm 65\text{ }\mu\text{m}$). Consistent with previous studies, we found that CC PCs have long, horizontal projections of axons across several barrel columns ($16500 \pm 3995\text{ }\mu\text{m}$ for axonal length and $1604 \pm 578\text{ }\mu\text{m}$ for axonal horizontal fieldspan). It should be noted that, for CC PCs, these values are likely to be highly underestimated because in acute brain slice preparations, long range axonal collaterals will be severely truncated (Egger et al. 2020); however, this does not prevent an unambiguous identification of the L6A PC type. In addition, PCs in cluster 3 exhibit long, sparsely tufted apical dendrites that reach layer 1 and exhibit horizontally expanding basal dendrites. A similar dendritic morphology has been found for IT claustrum-projecting neurons in layer 6 of rat and cat primary visual cortices (Katz 1987; Cotel et al. 2018) and are therefore named CClA PCs in the remainder of this manuscript. Here, these putative CClA PCs were found to have the largest vertical and horizontal dendritic fieldspan of the three L6A PC subtypes (Fig. 1D and Supplementary Table S1). Moreover, it is worth noting that CClA PCs have fewer basal dendrites compared with CT (3.6 ± 0.9 vs.

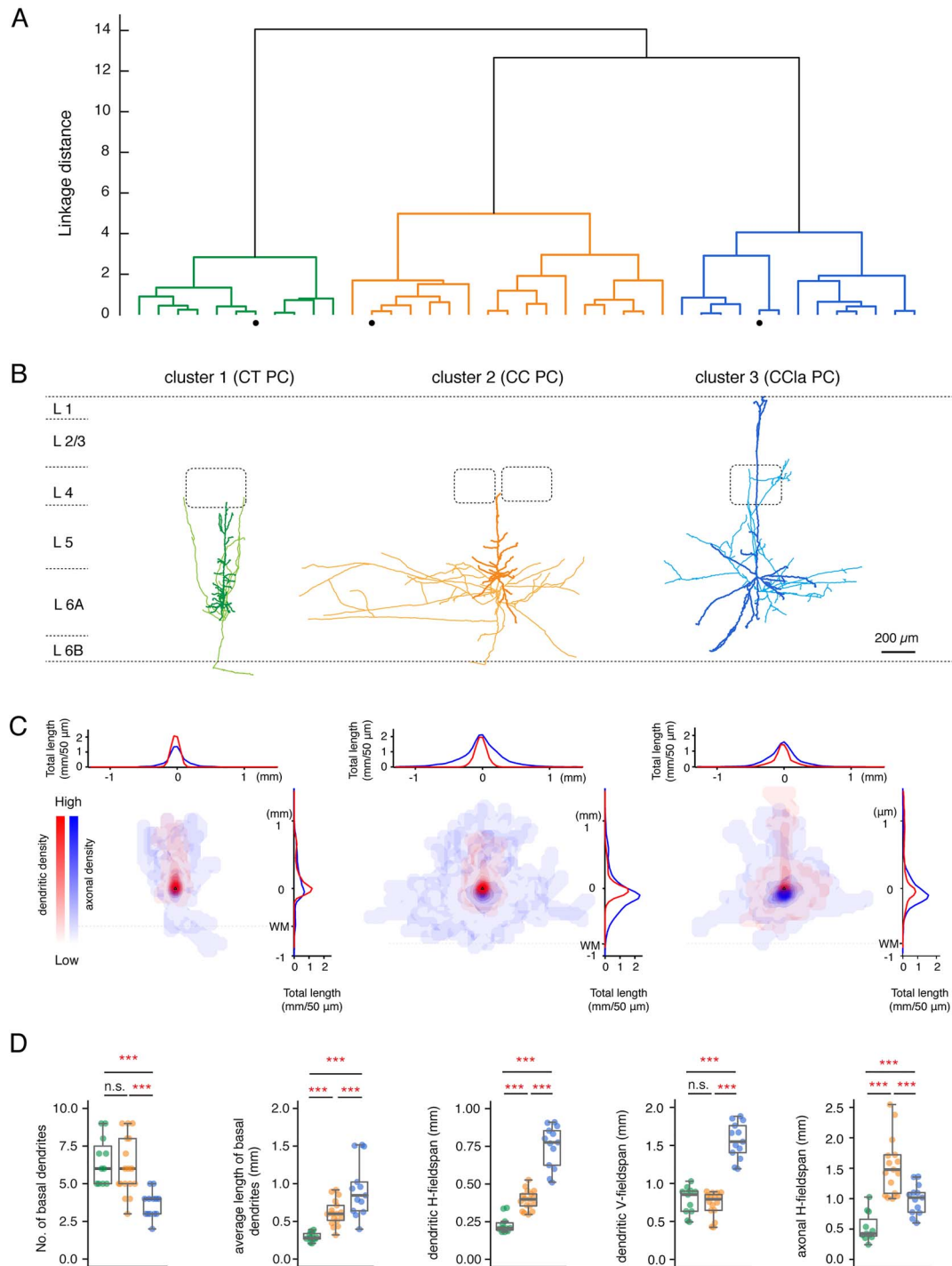


Figure 1. Identification of three morphological subtypes of PCs in L6A of rat barrel cortex. (A) An unsupervised hierarchical cluster analysis was used to identify different clusters from 41 L6A PCs based on morphological parameters. The morphological parameters that were used: number of basal dendrite, total length of basal dendrites, average length of basal dendrites, dendritic horizontal fieldspan, dendritic vertical fieldspan, axonal length, axonal horizontal fieldspan, and relative soma depth. (B) Representative morphological reconstructions of a CT (green) PC, a CC PC (orange), and a putative CClA PC (blue); the somatodendritic domain is given in a darker, the axons are in a lighter shade. Barrels and layer borders are indicated in dashed gray lines. (C) 2D density maps of L6A CT PCs (left, $n = 11$), CC PCs (center, $n = 17$), and CClA PCs (right, $n = 13$). Dendrites are shown in red and axons are shown in blue. Horizontal distribution of L6 PC dendrites and axons are shown on the top, while vertical distributions are shown on the right. The curves indicate the average dendritic and axonal density distribution; bin size in the x - and y -axes: 50 μ m in horizontal and vertical directions. Dashed lines indicate white matter position. (D) Summary data of several morphological properties of L6A CT ($n = 11$), CC ($n = 17$), and CClA ($n = 13$) PCs. Data are shown as box plots as described in the [Materials and Methods](#) section; individual points are color-coded as described above, *** $P < 0.001$, n.s. for $P \geq 0.05$ for the Wilcoxon Mann–Whitney U test; n.s., not significant.

6.6 ± 1.6 , $P = 6.4E-06$) and CC PCs (3.6 ± 0.9 vs. 6.1 ± 1.9 , $P = 6.9E-05$), but each single basal dendrite exhibits more collaterals that ramify profusely (average length of CClA PC basal dendrites: $929 \pm 370 \mu\text{m}$ vs. $295 \pm 59 \mu\text{m}$ for CT PCs and 617 ± 169 for CC PCs). The axonal length ($9564 \pm 4099 \mu\text{m}$) and horizontal field-span ($989 \pm 246 \mu\text{m}$) of CClA PCs range between those of CT and CC PCs (Fig. 1D). It has been found that the density of CClA projections is significantly higher in other cortical areas such as the prefrontal cortex (PFC), the anterior cingulate cortex, and association cortices (Atlan et al. 2017; White and Mathur 2018; Chia et al. 2020). Therefore, L6A CClA PCs should be found more frequently in the PFC than in the S1 barrel cortex. To examine this, we performed whole-cell recordings with simultaneous biocytin fillings from L6A excitatory neurons in rat PFC ($n = 173$). We found that the percentage of putative CClA PCs in layer 6A of the PFC was significantly larger in the PFC (18.5%) than in the barrel cortex (10.8%, see Supplementary Fig. S2).

Long-range axon collaterals of CC and CClA PCs are massively truncated in brain slice preparations. Therefore, axonal length and fieldspan measurements are severely underestimated (see, e.g., Egger et al. 2020). Despite this, the markedly distinct axonal and dendritic properties of the three L6A PC types allow an unambiguous cell-type identification. Density plots illustrating dendritic and axonal distributions of each PC type are shown in Figure 1C; individual reconstructions are depicted in Supplementary Figure S1. Additionally, we measured the relative distance from soma to pial surface to analyze the relationship between the laminar soma location and morphological patterns. We found that L6A CC and CClA PCs were located closer to the border between layers 5B and 6A, while CT PCs distribute preferentially in deeper layer 6A. More details regarding morphological properties and statistical comparisons are given in Supplementary Table S1.

In addition to their different morphological properties, L6A CT and CC PCs have been found to exhibit distinct passive and active electrophysiological characteristics (Kumar and Ohana 2008; Tian et al. 2014). Here, we systematically analyzed and compared the intrinsic electrophysiological properties of morphologically identified CT, CC, and putative CClA PCs. When compared with CC PCs, CT PCs showed a significantly higher input resistance and a shorter onset time for the first AP evoked by the rheobase current. CC PCs generally exhibit an initial spike burst composed of a doublet or triplet riding on a depolarizing envelope and display a larger first and second AP HWs (Fig. 2A and Supplementary Table S1). CClA PCs also showed a burst-like spiking pattern consisting of two initial, closely spaced spikes. However, in CC PCs, the second AP amplitude is smaller than that of the first AP, which is not the case in CClA PCs (Fig. 2A). In addition, CClA PCs display a significantly larger first AP amplitude than that of the other two PC types (102 ± 7 mV for CClA PCs, 93 ± 8 mV for CT PCs, and 92 ± 7 mV for CC PCs). Furthermore, putative CClA PCs showed the highest input resistance ($281 \pm 73 \text{ M}\Omega$ for CClA PCs, $235 \pm 80 \text{ M}\Omega$ for CT PCs, and $152 \pm 35 \text{ M}\Omega$ for CC PCs) and the most hyperpolarized AP threshold (-39.8 ± 3.3 mV for CClA PCs, -35.1 ± 3.5 for CT PCs, and -35.2 ± 3.5 for CC PCs) when injecting rheobase current (which was 63 ± 23 pA for CClA PCs, 118 ± 37 pA for CT PCs, and 133 ± 39 pA for CC PCs) (Fig. 2B). It needs to be noted that when the AP peak voltage is constant, the spike amplitude is negatively correlated with the spike threshold. Our results indicate that CClA PCs have a higher membrane excitability than the other L6A PC types. In conclusion, we were able to demonstrate that L6A PCs can

be reliably discriminated and classified on the basis of both morphological and physiological features as shown by the 3D scatter plot in Figure 2C. More electrophysiological properties and the statistical comparison of the three L6A PC types are shown in Figure 2D and Supplementary Table S1.

The nuclear transcription factor FoxP2 has been shown to be a molecular marker for CT L6A PCs (Hisaoka et al. 2010; Sundberg et al. 2018). To identify the expression of FoxP2 in L6A PCs, we performed whole-cell recordings with simultaneous filling of biocytin and the biocytin-conjugated fluorescent Alexa Fluor 594 dye. Subsequently, brain slices were processed for FoxP2 immunofluorescence staining. We found that the morphological and electrophysiological identified CT L6A PCs were FoxP2-positive, while both CC PCs and putative CClA PCs were FoxP2-negative (Supplementary Fig. S3). The correlation between neuronal morphology, electrophysiology, and FoxP2 expression demonstrates the reliability of our cell-type classification.

Specific Synaptic Properties of Presynaptic CT, CC, and CClA PCs Innervating Other L6A PCs

Because of the low excitatory synaptic connectivity ratio in layer 6A, a so-called “loose seal” searching protocol (see “Materials and Methods”) was used to test for potential synaptic connections. Hundred and ninety-four excitatory neurons were recorded as postsynaptic neurons, and 1513 potential presynaptic neurons were tested. Out of the tested cells, 96 were found to be synaptically coupled with the recorded excitatory neurons so that the connectivity ratio of L6A excitatory-to-excitatory (E→E) cell pairs was 6.3%. However, this value is likely to be an underestimate of the actual synaptic connectivity because of the high rate of axon truncations in brain slices.

Overall, 47 cell pairs were recorded successfully in dual whole-cell mode. After post hoc morphological reconstructions, the pre- and postsynaptic PC types were identified according to their specific features, as described in Figure 1. As in previous studies, the L6A bipolar, and inverted excitatory neurons were classified as CC PCs based on their horizontal axonal morphology and initial burst-spiking firing behavior (Zhang and Deschenes 1997; Kumar and Ohana 2008; for a review, see Thomson 2010). We found four synaptically coupled pairs with a presynaptic CT PC (3 CT→CT, 1 CT→CC), 36 pairs with a presynaptic CC PC (23 CC→CC, 13 CC→CT), and 7 pairs with a presynaptic CClA PC (6 CClA→CC, 1 CClA→CT). Morphological reconstructions and paired recordings of individual synaptically coupled neuron pairs are shown in Supplementary Figure S4.

As expected from their sparse axonal projection pattern, we found that presynaptic CT PCs rarely form synaptic connections with other L6A PCs (4 out of 47 pairs, 8.5%). Connections with CT PCs showed small amplitude unitary EPSPs (0.09 ± 0.10 mV) with a high CV (1.03 ± 0.25) and a high failure rate ($64.4 \pm 31.1\%$). Eliciting three APs in a presynaptic CT PC at an ISI of 100 ms resulted invariably in a strong short-term facilitation of the unitary synaptic response, as characterized by a mean $\text{PPR}_{\text{EPSP2/EPSP1}}$ of 2.22 ± 1.24 and $\text{PPR}_{\text{EPSP3/EPSP1}}$ of 1.89 ± 0.91 (Fig. 3A,B). In contrast to CT PCs, the vast majority of E→E connections were established by presynaptic CC PCs (36 out of 47 PCs, 76.6%). CC PCs were found to preferably innervate other CC PCs ($n = 23$) rather than CT PCs ($n = 13$) probably due to the smaller dendritic length and horizontal field-span of postsynaptic CT PCs (Fig. 1D). The E→E connections with a presynaptic CC PC displayed uEPSPs with an average amplitude of 0.37 ± 0.24 mV, which is significantly larger than

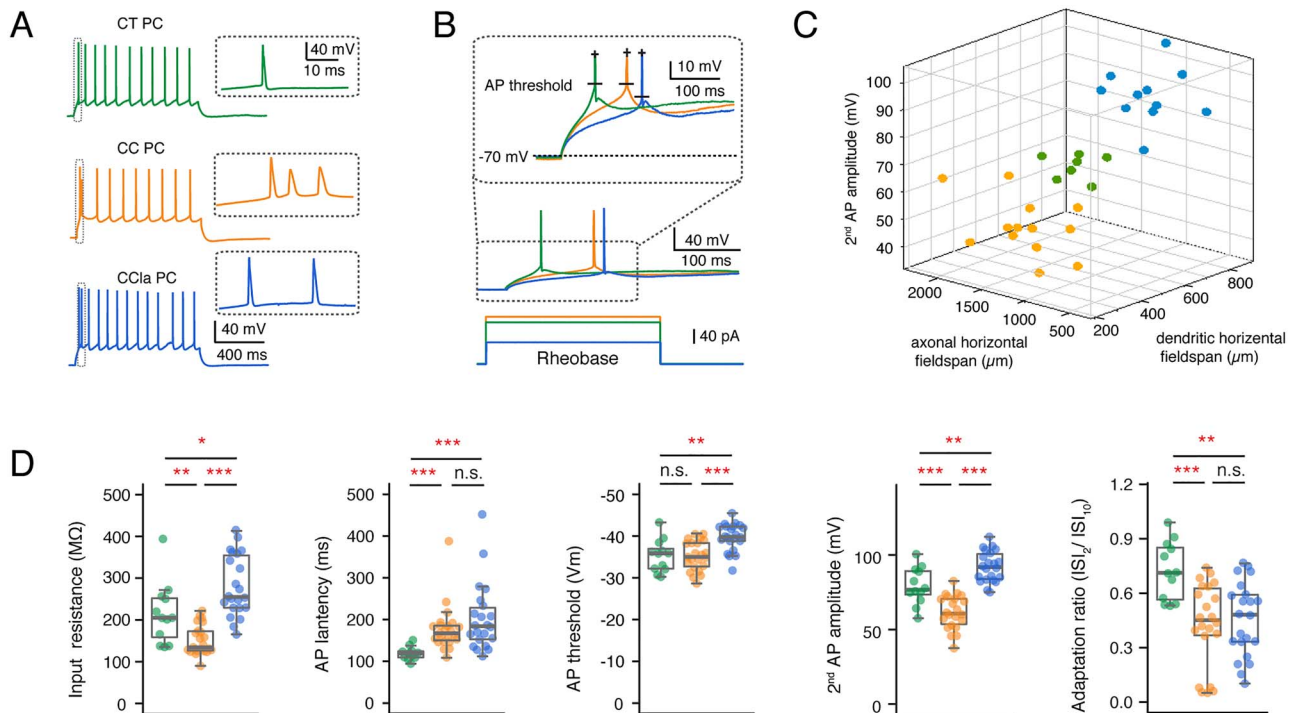


Figure 2. Comparison of electrophysiological parameters in morphological subtypes of L6A PCs. (A) Representative firing patterns of a morphological identified CT (green) PC, a CC PC (orange), and a putative CClA PC (blue); Inset, the initial part of the AP train at higher magnification. (B) First elicited AP (middle) of a representative CT (green), CC (orange), and CClA (blue) PC in response to rhebase current injection (bottom). Higher magnification of the first APs (inset) illustrating the difference in AP threshold and latency. (C) 3D scatter plot shows a clear separation of three L6A PC subtypes using morphological and electrophysiological properties. CT PCs in green, CC PCs in orange, and CClA PCs in blue. (D) Summary data of several electrophysiological properties of L6A CT ($n=15$), CC ($n=23$), and CClA ($n=22$) PCs. Data were compared between groups and were presented as box plots as described in the [Materials and Methods](#) section, $*P < 0.05$, $**P < 0.01$, $***P < 0.001$ for the Wilcoxon Mann-Whitney U test; n.s., not significant. The absolute P values are shown in [Supplementary Table S1](#).

that evoked by presynaptic CT PCs. The uEPSP amplitudes at this L6A connection type varied widely (from 0.03 to 0.98 mV) and exhibited either short-term depression or facilitation, which, on average, resulted in a paired-pulse ratio close to 1 ($PPR_{EPSP2/EPSP1}: 1.19 \pm 0.56$, $PPR_{EPSP3/EPSP1}: 1.08 \pm 0.39$) (Fig. 3A–C); the mean CV and failure rate were 0.68 ± 0.23 and $35.5 \pm 23.8\%$, respectively, suggesting that CC PCs form synapses of moderate efficacy (Fig. 3D). We also compared the functional properties of synaptic connections established by L6A CClA PCs. In contrast to the other two L6A PC subclasses, CClA PCs establish strong, reliable synaptic connections that displayed the largest average uEPSP amplitude (0.70 ± 0.40 mV), a comparatively small CV (0.57 ± 0.22), and a low failure rate ($18.8 \pm 18.9\%$). In response to a 10 Hz train of three APs elicited in a presynaptic CClA PC, EPSPs displayed short-term depression with a mean $PPR_{EPSP2/EPSP1}$ of 0.94 ± 0.25 and $PPR_{EPSP3/EPSP1}$ of 0.74 ± 0.21 (Fig. 3C,D). The difference in short-term synaptic plasticity between CT, CC, and CClA synaptic connections in layer 6A is even more evident in response to a train of 10 presynaptic APs ([Supplementary Fig. S5](#)). The EPSP latency, rise time, and decay time were similar for the different L6A connection types ([Table 1](#)).

To investigate whether synaptic properties depend also on the postsynaptic L6A PC subtype, we compared functional properties of morphologically identified CC→CC ($n=23$) and CC→CT ($n=11$) connections and found no significant difference in EPSP properties ([Supplementary Fig. S6](#)). Taken together, our results suggest that functional properties of E→E connections in layer 6A are presynaptic cell-type-specific but do not depend on the postsynaptic target neuron. A summary plot

of first EPSP amplitude versus presynaptic dendritic horizontal fieldspan is given in [Figure 3E](#), demonstrating a tight correlation between presynaptic neuron morphology and postsynaptic uEPSP properties.

We also studied the morphological characteristics of L6A synaptic connections between excitatory neurons (E→E connections). The average distance between the cell bodies of pre- and postsynaptic neurons is similar among the different connection types ([Table 1](#)), and no correlation between uEPSP amplitude and intersoma distance was found. To assess the number of putative synaptic contacts, we searched for close appositions of presynaptic axon terminals and postsynaptic dendrites under light microscopy ([Supplementary Fig. S7A–C](#)). Although it is likely that not all appositions are functional, a good correspondence has been shown previously between the axodendritic contacts identified with light microscopy and their verification by electron microscopy ([Silver et al. 2003](#); [Feldmeyer et al. 2006](#)). Comparison of the number of putative synaptic contacts between CT-, CC-, and CClA-formed connections revealed no marked difference ([Table 1](#) and [Supplementary Fig. S7E](#)). This suggests that differences in the number of synaptic contacts are probably not responsible for the cell-type-specific functional properties of L6A E→E connections. Considering the distinct short-term synaptic plasticity and difference in CV and failure rate, we conclude that presynaptic CT, CC, and CClA PCs show weak, moderate, and comparatively strong synaptic release probability, respectively, in synaptic connections with other L6A PCs. Moreover, light microscopic examination suggests that CT PCs established

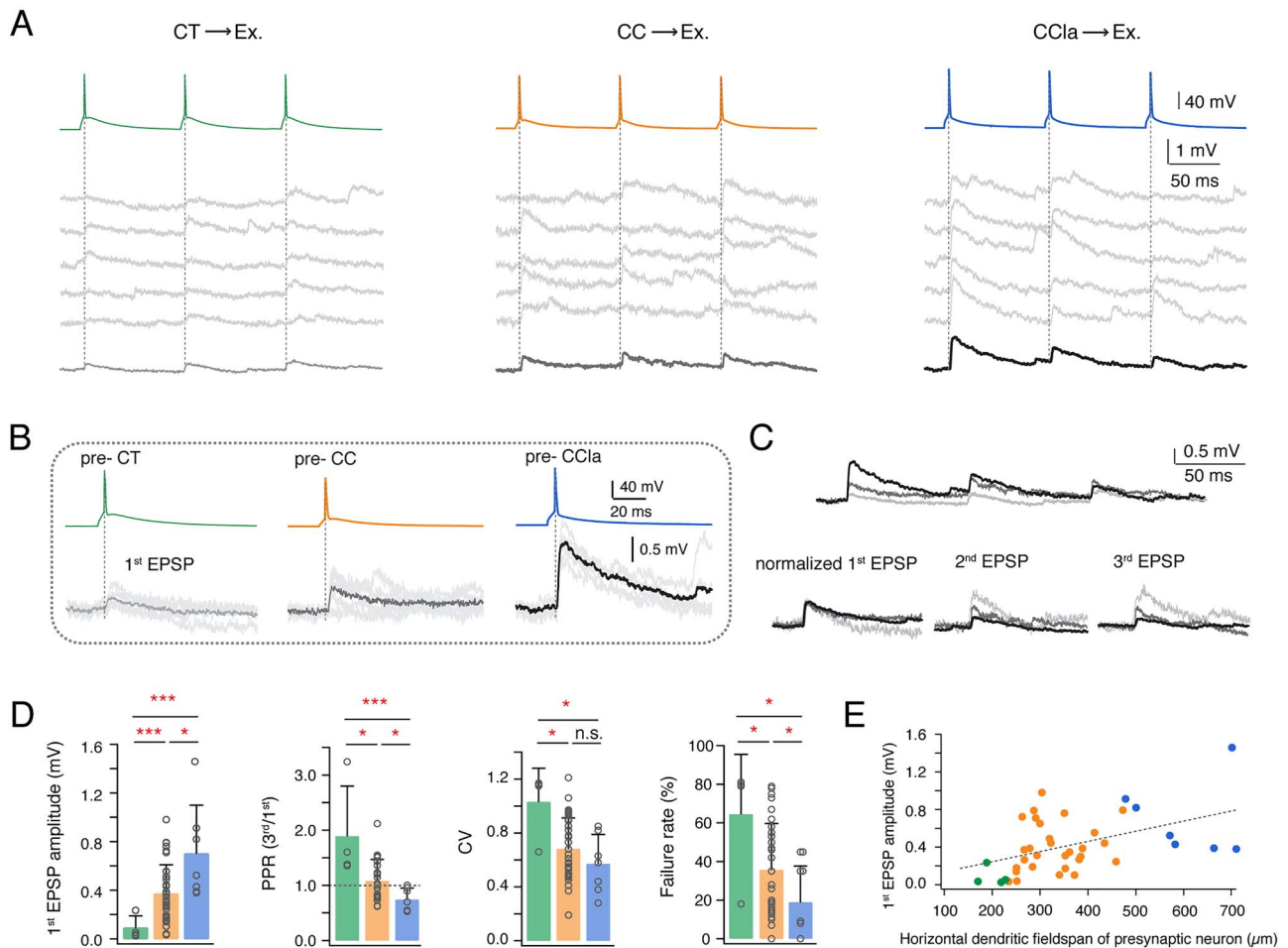


Figure 3. The properties of L6A E→E connections dependent on the different presynaptic PC subtypes. (A) Unitary synaptic connections in L6A with a presynaptic CT (left), CC (middle), and CClA (right) PC. Five consecutive EPSPs (middle) and the average EPSP (bottom) are elicited by a train of three presynaptic APs (top, 10 Hz). (B) First EPSP induced by AP of a presynaptic CT, CC, and CClA PC. The mean EPSP waveform is shown in light gray for pre-CT pair, in gray for pre-CC pair, and in dark gray for pre-CCla pair. (C) Top, overlay of average EPSPs recorded in a monosynaptic connection with a presynaptic CT (light gray), CC (gray), and CClA PC (dark gray). Bottom, normalizing the mean EPSP amplitudes reveals the difference in PPR for these three connection types. (D) Summary data of several synaptic properties of L6A E→E connections with presynaptic CT (green, $n=4$), CC (orange, $n=36$), and CClA (blue, $n=7$) PCs. Data were compared between groups and presented as the mean \pm SD, * $P < 0.05$, *** $P < 0.001$ for the Wilcoxon Mann–Whitney U test; n.s., not significant. (E) Plot of first EPSP amplitude versus horizontal dendritic field-span of the presynaptic neuron in L6A E→E connections. Best linear fit is shown as gray dashed line ($r=0.47$, $P=0.0014$). Color coding as in (D).

putative synaptic contacts on the proximal portion of the basal dendrites of L6A PCs with an average geometric distance of $65.3 \pm 36.8 \mu\text{m}$. For connections formed by CC PCs, putative synaptic contacts were found both on proximal and the distal portion of the basal dendrites, resulting in a significantly larger synapse-to-soma distance ($119.0 \pm 60.4 \mu\text{m}$) when compared with the connections with a presynaptic CC PC. L6A CClA PCs formed putative synapses on distal collaterals of basal dendrites and proximal apical oblique dendrites, displaying the largest average synapse-to-soma distance of $149.1 \pm 57.0 \mu\text{m}$ among the three L6A E→E connection types (Fig. S7D,E). These data suggest that for the different L6A E→E connections, despite a similar EPSP time course (Table 1), the location of synaptic contacts on postsynaptic dendrites is specific to the presynaptic cell type. However, we are well aware that light microscopic features do in general not predict whether a contact is actually synaptic or non-synaptic and that putative contacts formed by distal presynaptic axons are missed due to truncations (Holler et al. 2021). Nevertheless, light microscopy can provide

information when comparing synapse distributions for different neuron types obtained in the same study, as done here.

Characterization of PC-to-Interneuron Connections in Layer 6A of Rat Barrel Cortex

Neocortical GABAergic interneurons show a highly diverse firing pattern which depends largely on the interneuron type (Gupta et al. 2000; Ascoli et al. 2008; Yuste et al. 2020). Fast-spiking (FS) interneurons generate high-frequency APs without apparent frequency accommodation. The remaining interneurons are so-called nonfast-spiking (nFS) neurons, which comprise a large group of irregular-spiking, late spiking, and burst spiking interneurons (Kawaguchi and Kubota 1996; DeFelipe et al. 2013; Emmenegger et al. 2018). Both FS and nFS interneurons are broad families with different transcriptomic, electrophysiological, and morphological phenotypes (Gouwens et al. 2020; Scala et al. 2020; Yuste et al. 2020). Excitatory synapses onto FS interneurons are initially strong (i.e., have a high synaptic

Table 1 Functional and morphological properties of L6A E→E synaptic connections

	CT pairs (n = 4)	CC pairs (n = 36)	CCLa pairs (n = 7)	Kruskal- Wallis test	CT versus CC pairs	CT versus CCLa pairs	CC versus CCLa pairs
Electrophysiological properties							
Amplitude (mV)	0.09 ± 0.10 (0.03–0.24)	0.37 ± 0.24 (0.03–0.98)	0.70 ± 0.40 (0.38–1.46)	**0.0010	**0.0053	**0.0061	*0.0183
Paired-Pulse Ratio (second/first)	2.22 ± 1.24 (1.15–3.73)	1.19 ± 0.56 (0.62–3.21)	0.94 ± 0.25 (0.60–1.36)	*0.0499	*0.0358	*0.0242	0.0860
Paired-Pulse Ratio (third/first)	1.89 ± 0.91 (1.35–3.24)	1.08 ± 0.39 (0.62–2.12)	0.74 ± 0.21 (0.53–1.00)	**0.0042	*0.0234	**0.0061	*0.0282
CV	1.03 ± 0.25 (0.66–1.17)	0.68 ± 0.23 (0.37–1.21)	0.57 ± 0.22 (0.28–0.85)	*0.0268	*0.0143	*0.0242	0.2609
Failure rate (%)	64.4 ± 31.1 (18–81)	35.5 ± 23.8 (0–79)	18.8 ± 18.9 (0–45)	*0.0137	*0.0271	*0.0333	*0.0475
Rise time (ms)	0.91 ± 0.52 (0.24–1.52)	1.44 ± 0.99 (0.50–5.72)	1.44 ± 0.34 (1.14–1.96)	0.3434	0.3674	0.0697	0.4438
Latency (ms)	2.37 ± 0.86 (0.66–1.17)	1.73 ± 0.92 (0.80–4.67)	1.75 ± 0.70 (0.28–0.85)	0.2389	0.1150	0.2303	0.5681
Decay time (ms)	34.4 ± 26.1 (29.0–54.8)	38.8 ± 17.9 (12.7–73.1)	37.1 ± 9.0 (9.4–61.4)	0.8826	0.6878	0.8750	0.8586
Morphological properties							
No. of contacts per connection	3.3 ± 2.1 (1–5)	4.1 ± 1.8 (2–7)	3.8 ± 1.2 (2–5)	0.7090	0.7097	0.8810	0.4706
Geometric distance (μm)	65.3 ± 36.8 (36–150)	119.0 ± 60.4 (30–239)	149.1 ± 57.0 (36–237)	***6.2E-04	**0.0037	***0.0002	*0.0377
Intersoma distance (μm)	75.6 ± 92.3 (21–214)	78.1 ± 67.4 (20–345)	86.4 ± 77.1 (23–235)	0.1603	0.3004	0.2303	0.5589

Italic bold font indicates significant differences. Values in parentheses represent the smallest and largest values. * $P < 0.05$, ** $P < 0.01$, *** $P < 0.001$ for Kruskal–Wallis test among multiple groups followed by post hoc Wilcoxon Mann–Whitney U test between individual groups.

release probability) and depress with ongoing stimulation; excitatory synapses onto nFS neurons are generally weak (i.e., have a low synaptic release probability) and show facilitation upon repetitive firing (Tan et al. 2008; Caputi et al. 2009). In order to comprehensively investigate synaptic microcircuits between a L6A excitatory neuron and an inhibitory interneuron (E→I connection), we broadly classified L6A interneurons into a FS ($n = 23$) and an nFS ($n = 30$) group of interneurons on the basis of their electrophysiological properties. The characteristic feature of L6A FS interneurons was a high-frequency firing pattern with a low-frequency adaptation; nFS interneurons, on the other hand, were characterized by a low rheobase, high adaptation, and a lower firing frequency (Fig. 4A,B). Moreover, L6A FS and nFS interneurons also display significant differences in AP HW and afterhyperpolarization amplitude (Fig. 4C). The 3D scatter plots in Fig. 4D illustrate the reliability of the electrophysiological classification of these two L6A interneuron groups.

GABAergic interneurons in layer 6 of the neocortex show a high degree of morphological diversity (Kumar and Ohana 2008; Bortone et al. 2014; Arzt et al. 2018; Gouwens et al. 2019; Ding et al. 2020; Gouwens et al. 2020). In agreement with previous findings, heterogeneous axonal innervation profiles were identified for L6A FS and nFS interneurons, indicating that the firing behavior of L6A interneurons is not tightly correlated with their axonal projection patterns (Fig. 4E,F). While some were local interneurons with axonal collaterals confined to deep layers, others are interlaminar projecting interneurons with axons extending to more superficial layers. The axonal projections of most L6A interneuron types were not confined to the borders of the “home” cortical column, which, in layer 6, are delimited by the so-called L6 “infra-barrels” (Crandall et al. 2017) but innervated also neighboring “barrel columns” (Fig. 4E,F).

Paired recordings were performed between presynaptic L6A PCs and postsynaptic interneurons in layer 6A. Three hundred and sixty-nine potential connections were probed between presynaptic excitatory cells and postsynaptic interneurons. Thirty-nine excitatory synaptic connections were detected resulting in a connectivity ratio of 10.6%. For 33 E→I cell pairs, both presynaptic PCs and postsynaptic interneurons were morphologically reconstructed and electrophysiologically analyzed, allowing post hoc identification of connection subtypes in accordance with pre- and postsynaptic cell classes (Supplementary Fig. S8). As for E→E connections with a presynaptic CT PC, CT→interneuron connections were found to be weak (first EPSP amplitude ranging from 0.02 to 0.36 mV) and unreliable and displayed short-term facilitation (Fig. 5A,B). The functional properties of synaptic connections between CT PCs and FS or nFS interneurons were not significantly different. However, CT→FS connections tended to show slightly larger mean uEPSP amplitudes and weaker synaptic facilitation (Fig. 5C and Table 2). On the other hand, L6A FS and nFS interneurons showed distinct responses to presynaptic stimulation of CC PCs (Fig. 5A,B). Synaptic connections between CC PCs and (postsynaptic) L6A FS interneurons displayed short-term depression and a large mean uEPSP amplitude (1.13 ± 0.78 mV), low CV (0.62 ± 0.26), and low failure rate ($20.7 \pm 20.6\%$). In contrast, CC→nFS connections showed, on average, a small uEPSP amplitude (0.16 ± 0.18 mV), high CV (1.22 ± 0.28), and high failure rate ($59.0 \pm 24.3\%$) and exhibited short-term facilitation (Fig. 5C and Table 2). Similarly, a depression or facilitation of the postsynaptic response can be observed in CCLa→FS and CCLa→nFS connections, respectively (Supplementary Fig. S8). It is worth noting, however, that both FS and nFS interneurons show a large mean uEPSP amplitude and a low failure rate in

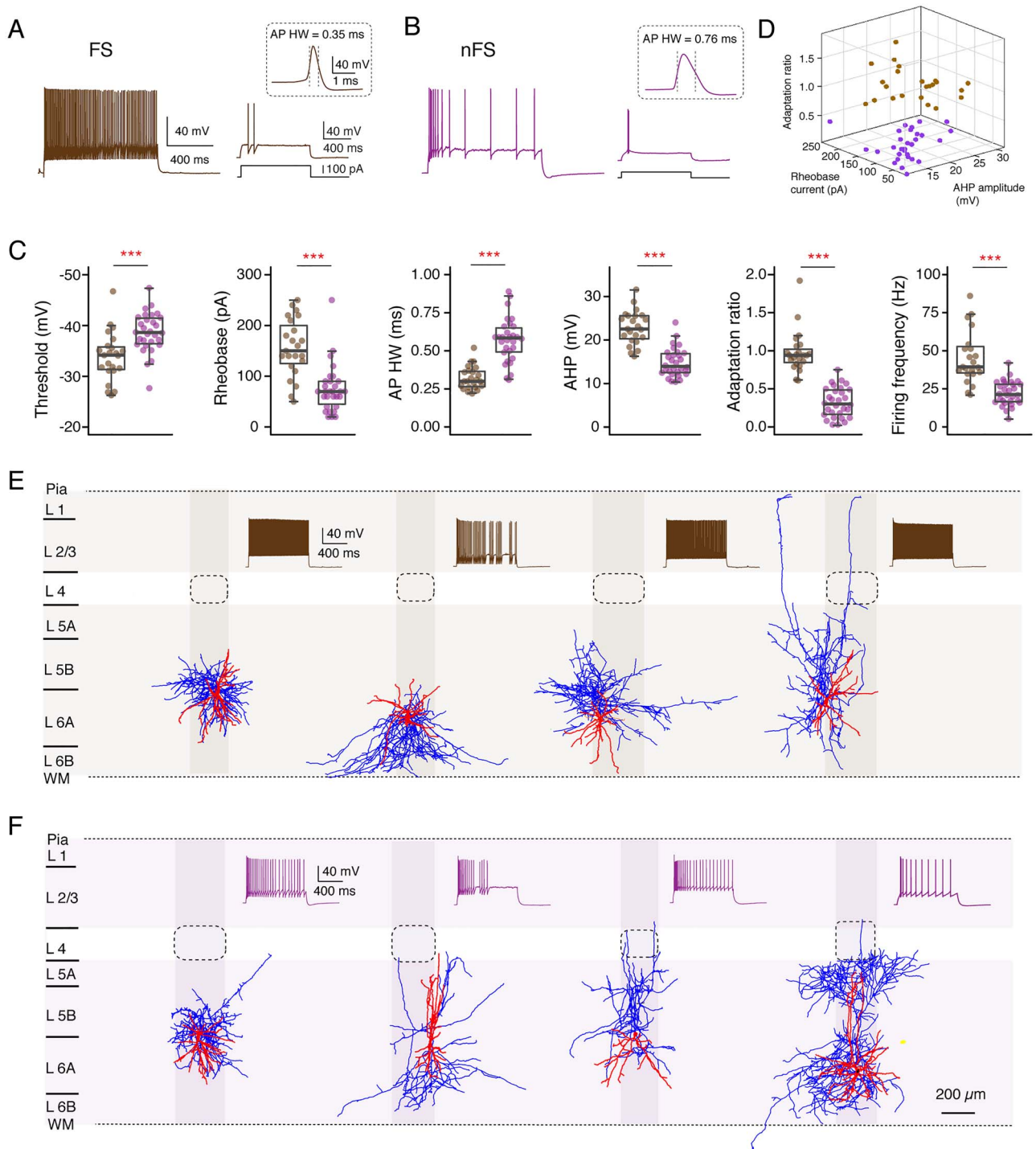


Figure 4. Two major electrophysiological interneuron subgroups in L6A of rat barrel cortex. (A, B) Left, representative firing patterns of a L6A FS (A) and an nFS (B) interneuron; the firing patterns for L6A nFS interneurons were highly variable. Right, responses of a FS and an nFS interneuron to rheobase current injection. The inset shows the first AP at higher magnification. (C) Summary data of several electrophysiological properties of L6A interneurons. Data were compared between groups and are presented as box plots as described in the Materials and Methods section, *** $P < 0.001$ for the Wilcoxon Mann–Whitney U test. (D) 3D scatter plot showing the clear separation of FS ($n = 23$) and nFS ($n = 30$) interneurons using electrophysiological properties. FS interneurons in brown and nFS interneurons in purple. (E, F) Representative morphological reconstructions and the corresponding firing patterns of four FS (E) and four nFS (F) interneurons. Both FS and nFS interneurons show diverse axonal projection patterns, suggesting that both groups comprise several different interneuron types. The somatodendritic domain is shown in red and axons are shown in blue. Barrels and home columns are indicated in light gray.

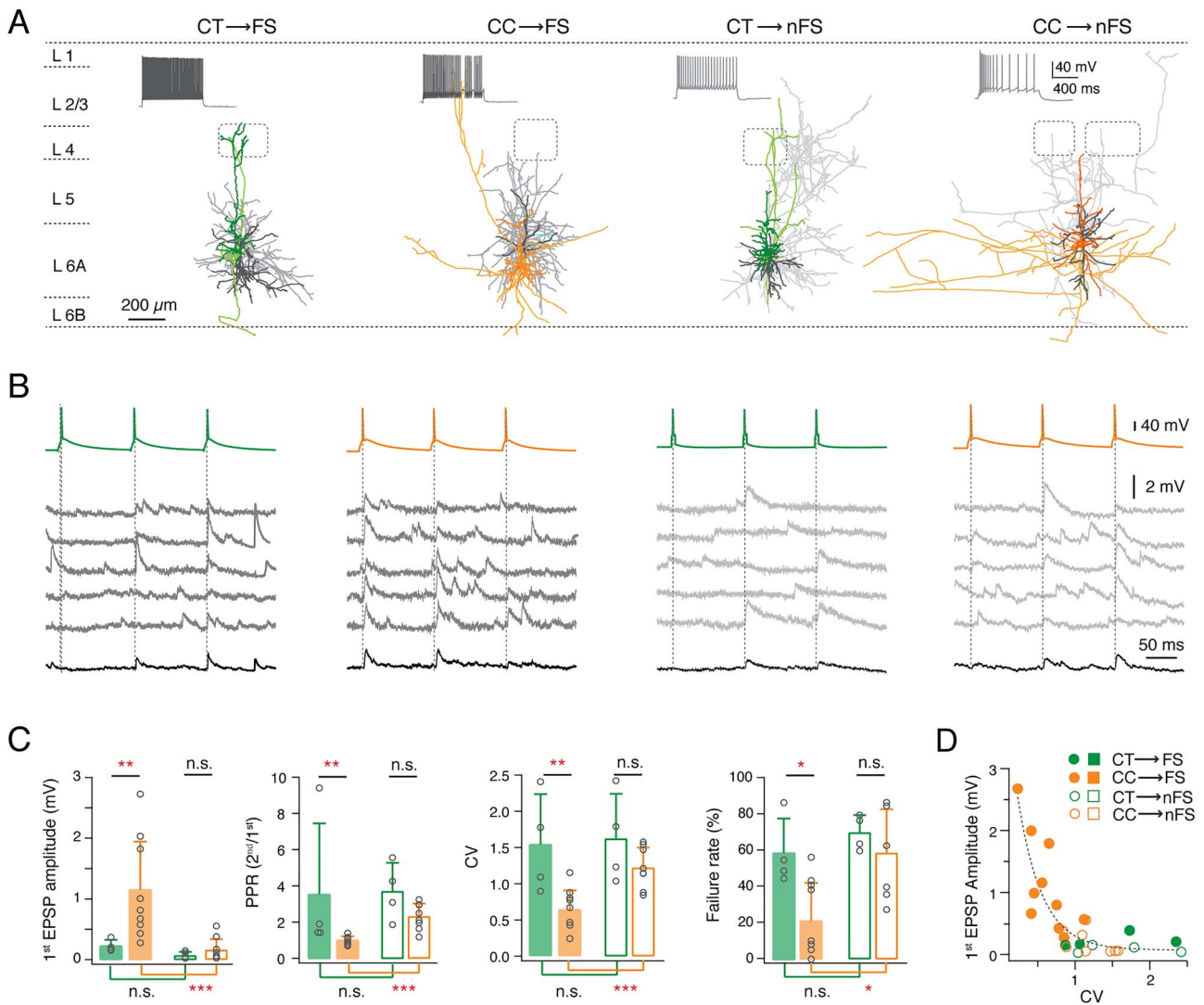


Figure 5. Both pre- and postsynaptic L6A neuron types govern synaptic characteristics of L6A E→I connections. (A) Representative morphological reconstructions of L6A CT→FS, CC→FS, CT→nFS, and CC→nFS synaptic connections. Neurons are shown in their approximate laminar location with respect to averaged cortical layers. The presynaptic somatodendritic domain is in a darker shade, the presynaptic axons in a lighter shade, postsynaptic soma and dendrites are in dark gray, and postsynaptic axons are in light gray. Barrels and layer borders are indicated by dashed gray lines. (B) Unitary synaptic connections obtained from CT→FS, CC→FS, CT→nFS, and CC→nFS pairs. Five consecutive EPSPs (middle) and average EPSP (bottom) were elicited by three consecutive presynaptic APs (top, interstimulus interval 100 ms). (C) Summary data of several synaptic properties of L6A E→I connections. Data were compared between groups and are presented as the mean ± SD, * $P < 0.05$, ** $P < 0.01$, *** $P < 0.001$ for the Wilcoxon Mann–Whitney U test; n.s., not significant. (D) Plot of the 1st uEPSP amplitude versus CV of L6A E→I connections. Note that the CC→FS connections have large EPSP amplitude and a small CV, while the other three E→I types are characterized by small mean uEPSP amplitudes and a large CV. Best linear and exponential fits are shown in gray dashed line.

response to presynaptic APs of CCl_a PC when compared to CT or CC PC (Table 2 and Supplementary Fig. S9). Statistical comparisons of other synaptic properties between different E→I connection types are given in Table 2. Our results indicate that both pre- and postsynaptic cell types govern synaptic characteristics in L6A E→I connections.

Discussion

It has been suggested that, in the neocortex, the laminar position of a neuronal cell body accounts for the differences in connection probability and short-term synaptic dynamics (Lefort and Petersen 2017; Seeman et al. 2018; Frandolig et al. 2019). However, for an in-depth understanding of the organization of

intralaminar connectivity in the neocortex, a thorough classification of the neuronal cell types in a given cortical layer is crucial (Kiritani et al. 2012; Kawaguchi 2017; Anastasiades et al. 2019; Whitesell et al. 2020). Here, we identified three distinct types of L6A PCs based on both their anatomical, electrophysiological, and synaptic features; these L6A PC types were named CT, CC, and putative CCl_a PCs based on their putative axonal targets. Previous studies of excitatory neuronal microcircuits in layer 6A of sensory cortices often overlooked CCl_a PCs (West et al. 2006; Crandall et al. 2017; Sundberg et al. 2018; Frandolig et al. 2019) probably because of their low density; in contrast, the abundance of CCl_a PCs is significantly larger in higher-order cortices such as the PFC (Gutierrez-Ibarluzea et al. 1999; Wang et al. 2017). Here, we were able to demonstrate that the three

Table 2 Functional properties of L6A E→I synaptic connections

	CT→FS (n=4)	CC→FS (n=9)	CCLa→FS (n=3)	CT→nFS (n=5)	CC→nFS (n=10)	CCLa→nFS (n=2)	Kruskal-Wallis test	CT→FS versus CC→FS	CT→nFS versus CC→nFS	CT→FS versus CT→nFS	CC→FS versus CC→nFS
Amplitude (mV)	0.22 ± 0.10	1.13 ± 0.78	2.84 ± 1.48	0.07 ± 0.06	0.16 ± 0.18	2.17, 1.03	***4.4E-07	**0.0040	0.2522	0.3095	***0.0002
PPR (second/first)	3.47 ± 3.83	0.99 ± 0.21	0.85 ± 0.20	3.72 ± 1.58	2.32 ± 0.72	1.15, 1.38	***1.3E-06	**0.0020	0.1535	0.3429	***9.1E-05
CV	1.50 ± 0.68	0.62 ± 0.26	0.30 ± 0.10	1.62 ± 0.62	1.22 ± 0.28	0.86, 0.57	***1.5E-05	**0.0070	0.2828	0.6857	***0.0003
Failure rate (%)	57.7 ± 18.7	20.7 ± 20.6	0.0 ± 0.0	70.2 ± 9.7	59.0 ± 24.3	27.7, 12.5	***4.8E-04	*0.0130	0.6485	0.3429	*0.0195
Rise time (ms)	0.50 ± 0.28	0.83 ± 0.25	0.69 ± 0.22	0.75 ± 0.74	1.12 ± 0.51	0.71, 0.61	0.2175	0.2000	0.3833	1.2000	0.1638
Latency (ms)	1.11 ± 0.52	1.03 ± 0.41	0.73 ± 0.52	1.85 ± 1.10	1.36 ± 0.58	0.88, 1.31	0.6007	0.5818	0.6303	0.8000	0.1388
Decay time (ms)	10.5 ± 1.7	12.3 ± 5.8	14.0 ± 10.6	16.9 ± 10.1	16.0 ± 5.7	14.3, 10.2	0.5177	0.9091	0.9048	1.2000	0.2977

Bold italic font indicates significant differences; *P < 0.05, **P < 0.01, ***P < 0.001 for Kruskal-Wallis test among multiple groups followed by post hoc Wilcoxon Mann-Whitney U test between individual groups.

L6A PC subpopulations establish excitatory synaptic connections with very distinct dynamic properties and may serve their differential functional roles.

CT PCs

In deep layers of the neocortex, principal neurons with projections confined to the telencephalon preferentially form synapses that show EPSP depression on repetitive stimulation, whereas ET-projecting PCs tend to display short-term facilitation (West et al. 2006; Le Be et al. 2007; Morishima et al. 2011; Cotel et al. 2018). In accordance with this view, our results showed that presynaptic CT PCs projecting to the ventral posterior medial nucleus (VPM) form excitatory connections that display strong short-term facilitation following repetitive stimulation (Killackey and Sherman 2003), while those formed by presynaptic intracortical CC PCs and putative CCLa PCs (i.e., IT-projecting L6A PCs) display only weak facilitation or depression. Apart from a population of remnant subplate neurons in layer 6 (Marx et al. 2017; Hoerder-Suabedissen et al. 2018), L6 CT PCs may be the earliest neuron class to populate the developing neocortex (Auladell et al. 2000). There is evidence that CC PCs in layer 6 of secondary somatosensory (S2) cortex are born later than CT PCs (Arimatsu et al. 1999; Arimatsu and Ishida 2002). With developmental maturation, glutamatergic synapses turn to short-term facilitation concomitant with a reduction in synaptic release probability (Oswald and Reyes 2008; Feldmeyer and Radnikow 2009). Thus, it is conceivable that the short-term facilitation of E→E connections reflects the degree of maturation of a synapse type; synapses formed by presynaptic CC and CCLa PCs are in a more immature state than L6A CT PCs and thus display more short-term depression (Fig. 6). Moreover, synaptotagmin-7 and synapsin I have been shown to play important functional roles in short-term synaptic facilitation at CT synapses (Nikolaev and Heggelund 2015; Jackman et al. 2016). If these molecules were also present at presynaptic terminals of “intracortical” connections established by CT PCs, this would explain—at least in part—EPSP facilitation at these synapses.

In accordance with previous studies (West et al. 2006; Cotel et al. 2018), we found that short-term facilitation is an important feature for the identification of L6A connections with a presynaptic CT PC regardless of the postsynaptic neuron type (Fig. 6). There are two known subgroups of L6 CT PCs in rat somatosensory cortex. A substantial fraction of L6A CT PCs located in deeper layer 6A projects to both the VPM and the posterior medial nucleus (PoM) of thalamus, while L6A CT PCs in upper L6A project predominantly to VPM alone (Zhang and Deschenes 1997; Killackey and Sherman 2003; Chevee et al. 2018). A recent study showed that unlike CT PCs projecting to VPM alone, those projecting to both VPM and PoM establish strong and depressing synapses with L6A PV-positive FS interneurons (Frändolig et al. 2019). Here, we did not find this specific connection type, probably because L6A CT PCs projecting to both VPM and PoM have a lower connection probability than the VPM-projecting L6A CT PC subtype (Frändolig et al. 2019). In addition, optogenetic stimulation of CT PCs resulted in facilitating synaptic responses in excitatory cells, FS, and nFS interneurons of layers 4 and 5 (Kim et al. 2014), suggesting that intra- and interlaminar connections with a presynaptic CT PC share common features.

CC PCs

Compared with L6A CT and CCLa PCs, CC PCs showed a higher connection probability with both other L6A PCs and interneurons. A fraction of the L6A CC PCs (~10%) was found to form

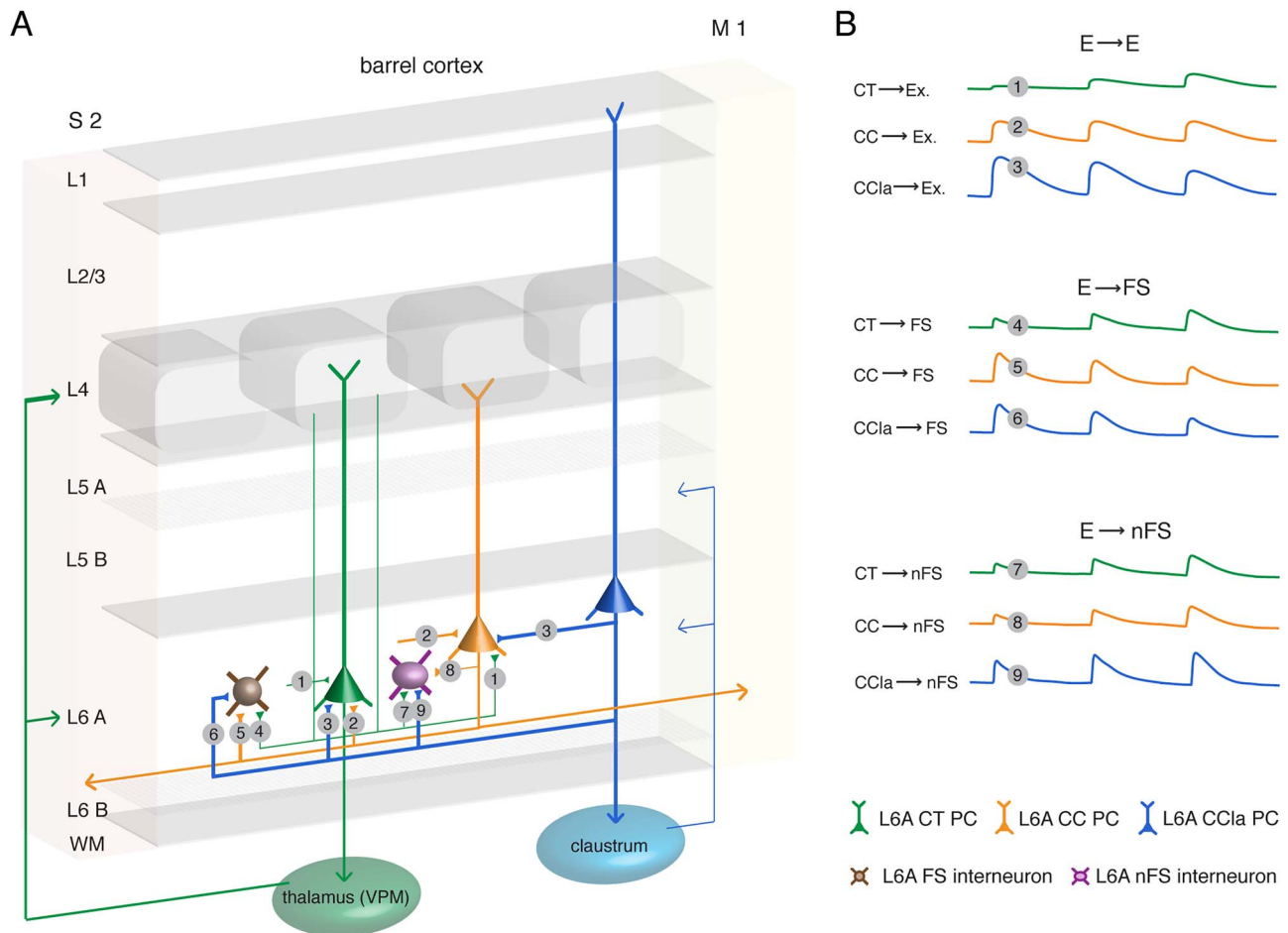


Figure 6. Schematic summary of the excitatory synaptic connections in L6A of rat barrel cortex. (A) Synaptic wiring scheme between L6A PCs ($E \rightarrow E$) and between L6A PC and interneuron ($E \rightarrow I$). The $E \rightarrow E$ morphological connection types obtained in this study are: CT \rightarrow CT (1), CT \rightarrow CC (1), CC \rightarrow CT (2), CC \rightarrow CC (2), CClA \rightarrow CT (3), and CClA \rightarrow CC (3) connections. The obtained $E \rightarrow I$ morphological connection types in this study are: CT \rightarrow FS (4), CC \rightarrow FS (5), CClA \rightarrow FS (6), CT \rightarrow nFS (7), CC \rightarrow nFS (8), and CClA \rightarrow nFS (9) connections. The thickness of axonal projection arrows indicates the efficacy of synaptic release. WM, white matter; S2, secondary somatosensory cortex; M1, primary motor cortex. (B) The first uEPSP amplitude and the short-term plasticity differ at the different L6A excitatory connection types. CT \rightarrow FS connections show no obvious short-term depression or facilitation. CC \rightarrow FS connections display a large first EPSP amplitude with short-term depression but establish weak and facilitating synapses with L6A nFS interneuron. CClA \rightarrow interneuron connections are strong, but CClA \rightarrow FS connections display short-term depression, while CClA \rightarrow nFS connections show short-term facilitation.

reciprocal synaptic connections with one another; however, for CT or CClA PCs, reciprocal connections were not detected. This suggests that intralaminar feedback excitation in layer 6A may be a neuronal cell-type-specific property (Morishima et al. 2011). Positive feedback excitation can drive a prolonged response to brief stimuli, thus maintaining burst activity (Grillner and Graybiel 2006; Li et al. 2006). During sensory processing, feedback excitation increases the sensitivity of CC PCs to thalamic inputs so that sensory signals can spread quickly and widely to neighboring barrel columns and even to other cortical areas (Douglas et al. 1995; Lim et al. 2012). On the other hand, studies using microiontophoretic injections demonstrated that the long, horizontally projecting axons of CC PCs form reciprocal synaptic connections across the somatosensory barrel cortex, the secondary somatosensory, the primary motor, and the perirhinal cortices (for a review, see Izraeli and Porter 1995; Zhang and Deschenes 1998; Aronoff et al. 2010). Here, we also detected several intercolumnar synaptic connections formed by CC PCs, with a lateral somatic distance of more than 200 μm ,

suggesting that they form not only local intralaminar synaptic microcircuits. This parallel organization of corticocortical connections in deep layers allows a fast convergence of thalamocortical inputs and in turn may drive reliable sensory responses (Egger et al. 2020).

L6A PC axons project throughout the entire barrel field and into adjacent cortices like the motor and S2 cortex and also extensively to superficial layers where they are likely to contact apical tufts of thick-tufted L5B and L2/3 PCs (Pichon et al. 2012; Egger et al. 2020). When proximal synaptic inputs to the basal dendrites of L5B PCs induce a somatic back-propagating APs, coincident synaptic input from L6A CC PCs to the apical tuft may sum with the back-propagating AP to trigger a dendritic calcium spike, a mechanism that is involved in the association of sensory inputs, perception, and learning (Larkum et al. 1999; Takahashi et al. 2016; Takahashi et al. 2020). Thus, L6A CC PCs may have important influence on synaptic integration of L5 PCs, amplifying the response to the thalamocortical inputs, while maintaining the neuronal selectivity (Hay and Segev 2015).

Putative CCl_a PCs

In rodents, almost all cortical areas have been found to provide synaptic input to the claustrum; in turn, the claustrum has axonal projections back to all ipsilateral cortical areas and to several contralateral cortical areas (Zakiewicz et al. 2014; Atlan et al. 2017). Although the claustrum is widely connected with different cortices, the density of CCl_a inputs varies considerably between different species and also different cortical areas (Zingg et al. 2018; Smith, Alloway, et al. 2019; Jackson et al. 2020) so that the functional role of the claustrum is not very well understood. It has been shown that the claustrum responds to stimuli of different sensory modalities and is therefore involved in processing sensory information (Remedios et al. 2010, 2014; Atlan et al. 2018). In the barrel cortex, CCl_a and claustrum-cortical axonal projections have been identified by retrograde tracing; they were found to originate or terminate, respectively, in deep layers (Zhang and Deschenes 1998; Atlan et al. 2017). The CCl_a PCs described here in layer 6A of rat barrel cortex are a homogeneous PC subpopulation both with respect to morphology and electrophysiology. They have ascending apical dendrites terminating in layer 1 and broad basal dendritic trees within layer 6, morphological features that are highly distinctive and similar to those of CCl_a PCs in cat and rat primary visual cortex (Katz 1987; Cotel et al. 2018). In layer 6A of rat PFC, a high percentage of PCs exhibit a tall, wide dendritic morphology, suggesting that this morphological subtype exist in many different cortical regions (van Aerde and Feldmeyer 2015). This is also in accordance with studies showing that the claustrum receives more extensive inputs from frontal cortical areas than the sensory cortices (Atlan et al. 2017; Zingg et al. 2018).

It is of note that the putative L6A CCl_a PCs identified here show a higher membrane excitability and stronger synaptic release than other L6A PC populations. This suggests that, although they form only a small fraction of L6A PCs, CCl_a PCs are actively involved in local circuits. L6A CCl_a PCs preferentially innervate CC rather than CT PCs and establish strong and reliable synaptic connections with both L6A PC classes. This suggests that they may contribute to the co-ordination of a wide-ranging network between different cortical regions. Furthermore, neocortical nFS interneurons appear to establish weak synaptic connections with neighboring PCs that show short-term facilitation, resulting in a delayed recruitment of inhibition via these interneurons (Helmstaedter et al. 2008; Caputi et al. 2009). This was also observed with CT→nFS and CC→nFS connections (Fig. 6). However, the putative CCl_a→nFS connections we recorded were also found to be strong and reliable, suggesting that the synaptic microcircuitry formed by L6A CCl_a PCs is uniquely salient.

Conclusion

In the neocortex, layer 6A not only receives strong thalamic input but has also been proposed to be the preeminent source of CT projections. This reciprocal pathway serves as a feedback loop so that thalamic neurons directly receive feedback from the innervating column. L6 CT PCs induced small, graded EPSPs that display paired-pulse facilitation; therefore, they are considered to modulate but not drive thalamic neurons (Reichova and Sherman 2004). The modulatory effect of CT inputs shifts from suppression to excitation depending on the activity frequency, thereby forming a dynamic top-down control of thalamic sensory processing (Crandall et al. 2015). CC PCs receive also extensive thalamic inputs (Pichon et al. 2012). Unlike CT synapses

that display always short-term facilitation, connections established by presynaptic CC PCs either showed weak facilitation or weak depression. The particular balance of short-term synaptic plasticity maintains the postsynaptic response in a steady-state, allowing a high-fidelity transmission of sensory information. Intracortical synapses established by L6A CCl_a PCs have a high neurotransmitter release probability resulting in large unitary EPSP that exhibit pronounced paired-pulse depression following repetitive stimulation. Because of this, CCl_a PCs may act as drivers of claustral neurons despite their sparseness in layer 6 of primary somatosensory cortex (Atlan et al. 2017; Chia et al. 2020). It has been shown that CCl_a afferents target both excitatory neurons and PV-positive interneurons in the claustrum (Kim et al. 2016; Chia et al. 2020). Feed-forward inhibition rapidly silences excitatory neurons, and only if inputs from several cortical regions arrive within a short time window, the claustrum-cortical pathway can be activated. The strong synaptic release of CCl_a inputs may contribute in this temporal convergence mechanism and serve in the integration of claustrum-cortical signaling from different sensorimotor areas (Smith and Alloway 2014). Hence, by establishing strong connections with claustral neurons and CC PCs in deep layers, L6 CCl_a PCs play an indispensable role in co-ordinating sensory and motor modalities from different cortical areas (Zingg et al. 2018; Chia et al. 2020).

In conclusion, we have demonstrated that excitatory synaptic microcircuits in layer 6A of rat barrel cortex are highly specific for the excitatory neuronal cell type, with important implications for intracortical network function and subcortical output of layer 6 as well as their feedback and feed-forward projections. Our study provides novel data necessary to obtain a more complete and coherent picture of the L6 microcircuitry and its role in cortical signaling pathways.

Supplementary Material

Supplementary material can be found at *Cerebral Cortex* online.

Funding

Helmholtz Society, the DFG Research Group—BaCoFun (grant no. Fe471/4-2 to D.F.); European Union's Horizon 2020 Research Innovation Programme (grant agreement no. 785907; HBP SGA2 to D.F.); China Scholarship Council (to D.Y. and C.D.).

Notes

We would like to thank Werner Hucko for excellent technical assistance and Dr Karlijn van Aerde for custom-written macros in Igor Pro software. We are also grateful to Dr Manuel Marx for sharing preliminary data for this project. We thank Carmen Kapitel and Jawad Jawadi for help with NeuroLucida reconstructions. *Conflict of Interest:* None declared.

References

- Agmon A, Connors BW. 1991. Thalamocortical responses of mouse somatosensory (barrel) cortex in vitro. *Neuroscience*. 41:365–379.
- Anastasiades PG, Boada C, Carter AG. 2019. Cell-type-specific D1 dopamine receptor modulation of projection neurons and interneurons in the prefrontal cortex. *Cereb Cortex*. 29:3224–3242.
- Arimatsu Y, Ishida M. 2002. Distinct neuronal populations specified to form corticocortical and corticothalamic projections

- from layer VI of developing cerebral cortex. *Neuroscience*. 114:1033–1045.
- Arimatsu Y, Ishida M, Sato M, Kojima M. 1999. Corticocortical associative neurons expressing latexin: specific cortical connectivity formed in vivo and in vitro. *Cereb Cortex*. 9:569–576.
- Aronoff R, Matyas F, Mateo C, Ciron C, Schneider B, Petersen CC. 2010. Long-range connectivity of mouse primary somatosensory barrel cortex. *Eur J Neurosci*. 31:2221–2233.
- Arzt M, Sakmann B, Meyer HS. 2018. Anatomical correlates of local, translaminal, and transcolumar inhibition by layer 6 GABAergic interneurons in somatosensory cortex. *Cereb Cortex*. 28:2763–2774.
- Ascoli GA, Alonso-Nanclares L, Anderson SA, Barrionuevo G, Benavides-Piccione R, Burkhalter A, Buzsáki G, Cauli B, Defelipe J, Fairen A, et al. 2008. Petilla terminology: nomenclature of features of GABAergic interneurons of the cerebral cortex. *Nat Rev Neurosci*. 9:557–568.
- Atlan G, Terem A, Peretz-Rivlin N, Groysman M, Citri A. 2017. Mapping synaptic cortico-claustral connectivity in the mouse. *J Comp Neurol*. 525:1381–1402.
- Atlan G, Terem A, Peretz-Rivlin N, Sehrawat K, Gonzales BJ, Pozner G, Tasaka GI, Goll Y, Refaeli R, Zviran O, et al. 2018. The claustrum supports resilience to distraction. *Curr Biol*. 28:2752–2762 e2757.
- Auladell C, Perez-Sust P, Super H, Soriano E. 2000. The early development of thalamocortical and corticothalamic projections in the mouse. *Anat Embryol*. 201:169–179.
- Baker A, Kalmbach B, Morishima M, Kim J, Juavinett A, Li N, Dembrow N. 2018. Specialized subpopulations of deep-layer pyramidal neurons in the neocortex: bridging cellular properties to functional consequences. *J Neurosci*. 38:5441–5455.
- Bayat A, Joshi S, Jahan S, Connell P, Tsuchiya K, Chau D, Syed T, Forcelli P, Koubeissi MZ. 2018. A pilot study of the role of the claustrum in attention and seizures in rats. *Epilepsy Res*. 140:97–104.
- Beierlein M, Connors BW. 2002. Short-term dynamics of thalamocortical and intracortical synapses onto layer 6 neurons in neocortex. *J Neurophysiol*. 88:1924–1932.
- Bortone DS, Olsen SR, Scanziani M. 2014. Translaminal inhibitory cells recruited by layer 6 corticothalamic neurons suppress visual cortex. *Neuron*. 82:474–485.
- Caputi A, Rozov A, Blatow M, Monyer H. 2009. Two calretinin-positive GABAergic cell types in layer 2/3 of the mouse neocortex provide different forms of inhibition. *Cereb Cortex*. 19:1345–1359.
- Chevee M, Robertson JJ, Cannon GH, Brown SP, Goff LA. 2018. Variation in activity state, axonal projection, and position define the transcriptional identity of individual neocortical projection neurons. *Cell Rep*. 22:441–455.
- Chia Z, Augustine GJ, Silberberg G. 2020. Synaptic connectivity between the cortex and claustrum is organized into functional modules. *Curr Biol*. 30:2777–2790 e2774.
- Clancy B, Cauller LJ. 1999. Widespread projections from subgriseal neurons (layer VII) to layer I in adult rat cortex. *J Comp Neurol*. 407:275–286.
- Cotel F, Fletcher LN, Kalita-de Croft S, Apergis-Schoute J, Williams SR. 2018. Cell class-dependent intracortical connectivity and output dynamics of layer 6 projection neurons of the rat primary visual cortex. *Cereb Cortex*. 28:2340–2350.
- Crandall SR, Cruikshank SJ, Connors BW. 2015. A corticothalamic switch: controlling the thalamus with dynamic synapses. *Neuron*. 86:768–782.
- Crandall SR, Patrick SL, Cruikshank SJ, Connors BW. 2017. Infrabarrels are layer 6 circuit modules in the barrel cortex that link long-range inputs and outputs. *Cell Rep*. 21:3065–3078.
- DeFelipe J, Lopez-Cruz PL, Benavides-Piccione R, Bielza C, Larranaga P, Anderson S, Burkhalter A, Cauli B, Fairen A, Feldmeyer D, et al. 2013. New insights into the classification and nomenclature of cortical GABAergic interneurons. *Nat Rev Neurosci*. 14:202–216.
- Ding C, Emmenegger V, Schaffrath K, Feldmeyer D. 2020. Layer-specific inhibitory microcircuits of layer 6 interneurons in rat prefrontal cortex. *Cereb Cortex*. 31:32–47.
- Douglas RJ, Koch C, Mahowald M, Martin KA, Suarez HH. 1995. Recurrent excitation in neocortical circuits. *Science*. 269:981–985.
- Egger R, Narayanan RT, Guest JM, Bast A, Udvary D, Messori LF, Das S, de Kock CPJ, Oberlaender M. 2020. Cortical output is gated by horizontally projecting neurons in the deep layers. *Neuron*. 105:122–137 e128.
- Emmenegger V, Qi G, Wang H, Feldmeyer D. 2018. Morphological and functional characterization of non-fast-spiking GABAergic interneurons in layer 4 microcircuitry of rat barrel cortex. *Cereb Cortex*. 28:1439–1457.
- Feldmeyer D, Egger V, Lubke J, Sakmann B. 1999. Reliable synaptic connections between pairs of excitatory layer 4 neurones within a single 'barrel' of developing rat somatosensory cortex. *J Physiol*. 521(Pt 1):169–190.
- Feldmeyer D, Lübke J, Sakmann B. 2006. Efficacy and connectivity of intracolumnar pairs of layer 2/3 pyramidal cells in the barrel cortex of juvenile rats. *J Physiol*. 575:583–602.
- Feldmeyer D, Lubke J, Silver RA, Sakmann B. 2002. Synaptic connections between layer 4 spiny neurone-layer 2/3 pyramidal cell pairs in juvenile rat barrel cortex: physiology and anatomy of interlaminar signalling within a cortical column. *J Physiol*. 538:803–822.
- Feldmeyer D, Radnikow G. 2009. Developmental alterations in the functional properties of excitatory neocortical synapses. *J Physiol*. 587:1889–1896.
- Feldmeyer D, Radnikow G. 2016. Paired recordings from synaptically coupled neurones in acute neocortical slices. In: Kornegreen A, editor. *Advanced patch-clamp analysis for neuroscientists*. Springer Science+Business Media: New York, pp. 171–191.
- Frändolig JE, Matney CJ, Lee K, Kim J, Chevee M, Kim SJ, Bickert AA, Brown SP. 2019. The synaptic organization of layer 6 circuits reveals inhibition as a major output of a neocortical sublamina. *Cell Rep*. 28:3131–3143 e3135.
- Gouwens NW, Sorensen SA, Baftizadeh F, Budzillo A, Lee BR, Jarsky T, Alfiler L, Baker K, Barkan E, Berry K, et al. 2020. Integrated morphoelectric and transcriptomic classification of cortical GABAergic cells. *Cell*. 183:935–953 e919.
- Gouwens NW, Sorensen SA, Berg J, Lee C, Jarsky T, Ting J, Sunkin SM, Feng D, Anastassiou CA, Barkan E, et al. 2019. Classification of electrophysiological and morphological neuron types in the mouse visual cortex. *Nat Neurosci*. 22:1182–1195.
- Grillner S, Graybiel AM. 2006. *Microcircuits: the interface between neurons and global brain function*. Cambridge (MA): MIT Press in cooperation with Dahlem University Press.
- Gupta A, Wang Y, Markram H. 2000. Organizing principles for a diversity of GABAergic interneurons and synapses in the neocortex. *Science*. 287:273–278.
- Gutierrez-Ibarluzea I, Acera-Osa A, Mendizabal-Zubiaga JL, Arana-Arri E, Bueno-Lopez JL, Reblet C. 1999. Morphology and

- laminar distribution of cortico-claustral neurons in different areas of the rabbit cerebral cortex. *Eur J Anat.* 3:101–109.
- Harris KD, Mrsic-Flogel TD. 2013. Cortical connectivity and sensory coding. *Nature.* 503:51–58.
- Hay E, Segev I. 2015. Dendritic excitability and gain control in recurrent cortical microcircuits. *Cereb Cortex.* 25:3561–3571.
- Helmstaedter M, Staiger JF, Sakmann B, Feldmeyer D. 2008. Efficient recruitment of layer 2/3 interneurons by layer 4 input in single columns of rat somatosensory cortex. *J Neurosci.* 28:8273–8284.
- Hisaoka T, Nakamura Y, Senba E, Morikawa Y. 2010. The forkhead transcription factors, Foxp1 and Foxp2, identify different subpopulations of projection neurons in the mouse cerebral cortex. *Neuroscience.* 166:551–563.
- Hoerder-Suabedissen A, Hayashi S, Upton L, Nolan Z, Casas-Torremocha D, Grant E, Viswanathan S, Kanold PO, Clasca F, Kim Y, et al. 2018. Subset of cortical layer 6b neurons selectively innervates higher order thalamic nuclei in mice. *Cereb Cortex.* 28:1882–1897.
- Hoerder-Suabedissen A, Oeschger FM, Krishnan ML, Belgard TG, Wang WZ, Lee S, Webber C, Petretto E, Edwards AD, Molnar Z. 2013. Expression profiling of mouse subplate reveals a dynamic gene network and disease association with autism and schizophrenia. *Proc Natl Acad Sci U S A.* 110:3555–3560.
- Hoerder-Suabedissen A, Wang WZ, Lee S, Davies KE, Goffinet AM, Rakic S, Parnavelas J, Reim K, Nicolic M, Paulsen O, et al. 2009. Novel markers reveal subpopulations of subplate neurons in the murine cerebral cortex. *Cereb Cortex.* 19:1738–1750.
- Holler S, Kostinger G, Martin KAC, Schuhknecht GFP, Stratford KJ. 2021. Structure and function of a neocortical synapse. *Nature.* 591:111–116.
- Hutsler JJ, Lee DG, Porter KK. 2005. Comparative analysis of cortical layering and supragranular layer enlargement in rodent carnivore and primate species. *Brain Res.* 1052:71–81.
- Izraeli R, Porter LL. 1995. Vibrissal motor cortex in the rat: connections with the barrel field. *Exp Brain Res.* 104:41–54.
- Jackman SL, Turecek J, Belinsky JE, Regehr WG. 2016. The calcium sensor synaptotagmin 7 is required for synaptic facilitation. *Nature.* 529:88–91.
- Jackson J, Smith JB, Lee AK. 2020. The anatomy and physiology of claustrum-cortex interactions. *Annu Rev Neurosci.* 43:231–247.
- Kast RJ, Lanjewar AL, Smith CD, Levitt P. 2019. FOXP2 exhibits projection neuron class specific expression, but is not required for multiple aspects of cortical histogenesis. *Elife.* 8:e42012.
- Katz LC. 1987. Local circuitry of identified projection neurons in cat visual cortex brain slices. *J Neurosci.* 7:1223–1249.
- Kawaguchi Y. 2017. Pyramidal cell subtypes and their synaptic connections in layer 5 of rat frontal cortex. *Cereb Cortex.* 27:5755–5771.
- Kawaguchi Y, Kubota Y. 1996. Physiological and morphological identification of somatostatin- or vasoactive intestinal polypeptide-containing cells among GABAergic cell subtypes in rat frontal cortex. *J Neurosci.* 16:2701–2715.
- Killackey HP, Sherman SM. 2003. Corticothalamic projections from the rat primary somatosensory cortex. *J Neurosci.* 23:7381–7384.
- Kim J, Matney CJ, Blankenship A, Hestrin S, Brown SP. 2014. Layer 6 corticothalamic neurons activate a cortical output layer, layer 5a. *J Neurosci.* 34:9656–9664.
- Kim J, Matney CJ, Roth RH, Brown SP. 2016. Synaptic organization of the neuronal circuits of the claustrum. *J Neurosci.* 36:773–784.
- Kiritani T, Wickersham IR, Seung HS, Shepherd GM. 2012. Hierarchical connectivity and connection-specific dynamics in the corticospinal-corticoatrial microcircuit in mouse motor cortex. *J Neurosci.* 32:4992–5001.
- Kumar P, Ohana O. 2008. Inter- and intralaminar subcircuits of excitatory and inhibitory neurons in layer 6a of the rat barrel cortex. *J Neurophysiol.* 100:1909–1922.
- Larkum ME, Zhu JJ, Sakmann B. 1999. A new cellular mechanism for coupling inputs arriving at different cortical layers. *Nature.* 398:338–341.
- Le Be JV, Silberberg G, Wang Y, Markram H. 2007. Morphological, electrophysiological, and synaptic properties of corticocortical pyramidal cells in the neonatal rat neocortex. *Cereb Cortex.* 17:2204–2213.
- Lefort S, Petersen CCH. 2017. Layer-dependent short-term synaptic plasticity between excitatory neurons in the C2 barrel column of mouse primary somatosensory cortex. *Cereb Cortex.* 27:3869–3878.
- Li WC, Soffe SR, Wolf E, Roberts A. 2006. Persistent responses to brief stimuli: feedback excitation among brainstem neurons. *J Neurosci.* 26:4026–4035.
- Lim DH, Mohajerani MH, Ledue J, Boyd J, Chen S, Murphy TH. 2012. In vivo large-scale cortical mapping using channelrhodopsin-2 stimulation in transgenic mice reveals asymmetric and reciprocal relationships between cortical areas. *Front Neural Circuits.* 6:11.
- Lodato S, Arlotta P. 2015. Generating neuronal diversity in the mammalian cerebral cortex. *Annu Rev Cell Dev Biol.* 31:699–720.
- Marx M, Feldmeyer D. 2013. Morphology and physiology of excitatory neurons in layer 6b of the somatosensory rat barrel cortex. *Cereb Cortex.* 23:2803–2817.
- Marx M, Gunter RH, Hucko W, Radnikow G, Feldmeyer D. 2012. Improved biocytin labeling and neuronal 3D reconstruction. *Nat Protoc.* 7:394–407.
- Marx M, Qi G, Hanganu-Opatz IL, Kilb W, Luhmann HJ, Feldmeyer D. 2017. Neocortical layer 6B as a remnant of the subplate—a morphological comparison. *Cereb Cortex.* 27:1011–1026.
- Mercer A, West DC, Morris OT, Kirchhecker S, Kerkhoff JE, Thomson AM. 2005. Excitatory connections made by presynaptic cortico-cortical pyramidal cells in layer 6 of the neocortex. *Cereb Cortex.* 15:1485–1496.
- Meyer HS, Wimmer VC, Hemberger M, Bruno RM, de Kock CP, Frick A, Sakmann B, Helmstaedter M. 2010. Cell type-specific thalamic innervation in a column of rat vibrissal cortex. *Cereb Cortex.* 20:2287–2303.
- Morishima M, Morita K, Kubota Y, Kawaguchi Y. 2011. Highly differentiated projection-specific cortical subnetworks. *J Neurosci.* 31:10380–10391.
- Naghavi HR, Eriksson J, Larsson A, Nyberg L. 2007. The claustrum/insula region integrates conceptually related sounds and pictures. *Neurosci Lett.* 422:77–80.
- Nikolaev M, Heggelund P. 2015. Functions of synapsins in corticothalamic facilitation: important roles of synapsin I. *J Physiol.* 593:4499–4510.
- Oeschger FM, Wang WZ, Lee S, Garcia-Moreno F, Goffinet AM, Arbones ML, Rakic S, Molnar Z. 2012. Gene expression analysis of the embryonic subplate. *Cereb Cortex.* 22:1343–1359.
- Oswald AM, Reyes AD. 2008. Maturation of intrinsic and synaptic properties of layer 2/3 pyramidal neurons in mouse auditory cortex. *J Neurophysiol.* 99:2998–3008.

- Peters SK, Dunlop K, Downar J. 2016. Cortico-striatal-thalamic loop circuits of the salience network: a central pathway in psychiatric disease and treatment. *Front Syst Neurosci.* 10:104.
- Pichon F, Nikonenko I, Kraftsik R, Welker E. 2012. Intracortical connectivity of layer VI pyramidal neurons in the somatosensory cortex of normal and barrelless mice. *Eur J Neurosci.* 35:855–869.
- Rakic P. 2009. Evolution of the neocortex: a perspective from developmental biology. *Nat Rev Neurosci.* 10:724–735.
- Reichova I, Sherman SM. 2004. Somatosensory corticothalamic projections: distinguishing drivers from modulators. *J Neurophysiol.* 92:2185–2197.
- Remedios R, Logothetis NK, Kayser C. 2010. Unimodal responses prevail within the multisensory claustrum. *J Neurosci.* 30:12902–12907.
- Remedios R, Logothetis NK, Kayser C. 2014. A role of the claustrum in auditory scene analysis by reflecting sensory change. *Front Syst Neurosci.* 8:44.
- Rockland KS. 2019. What do we know about laminar connectivity? *Neuroimage.* 197:772–784.
- Scala F, Kobak D, Bernabucci M, Bernaerts Y, Cadwell CR, Castro JR, Hartmanis L, Jiang X, Laturus S, Miranda E, et al. 2021. Phenotypic variation of transcriptomic cell types in mouse motor cortex. *Nature.* 598:144–150.
- Seeman SC, Campagnola L, Davoudian PA, Hoggarth A, Hage TA, Bosma-Moody A, Baker CA, Lee JH, Mihalas S, Teeter C, et al. 2018. Sparse recurrent excitatory connectivity in the microcircuit of the adult mouse and human cortex. *Elife.* 7:e37349.
- Silver RA, Lubke J, Sakmann B, Feldmeyer D. 2003. High-probability uniquantal transmission at excitatory synapses in barrel cortex. *Science.* 302:1981–1984.
- Smith JB, Alloway KD. 2014. Interhemispheric claustral circuits coordinate sensory and motor cortical areas that regulate exploratory behaviors. *Front Syst Neurosci.* 8:93.
- Smith JB, Alloway KD, Hof PR, Orman R, Reser DH, Watakabe A, Watson GDR. 2019. The relationship between the claustrum and endopiriform nucleus: a perspective towards consensus on cross-species homology. *J Comp Neurol.* 527:476–499.
- Smith JB, Liang Z, Watson GDR, Alloway KD, Zhang N. 2017. Interhemispheric resting-state functional connectivity of the claustrum in the awake and anesthetized states. *Brain Struct Funct.* 222:2041–2058.
- Smith JB, Watson GDR, Liang Z, Liu Y, Zhang N, Alloway KD. 2019. A role for the claustrum in salience processing? *Front Neuroanat.* 13:64.
- Sundberg SC, Lindstrom SH, Sanchez GM, Granseth B. 2018. Cre-expressing neurons in visual cortex of Ntsr1-Cre GN220 mice are corticothalamic and are depolarized by acetylcholine. *J Comp Neurol.* 526:120–132.
- Takahashi N, Ebner C, Sigl-Glockner J, Moberg S, Nierwetberg S, Larkum ME. 2020. Active dendritic currents gate descending cortical outputs in perception. *Nat Neurosci.* 23:1277–1285.
- Takahashi N, Oertner TG, Hegemann P, Larkum ME. 2016. Active cortical dendrites modulate perception. *Science.* 354:1587–1590.
- Tan Z, Hu H, Huang ZJ, Agmon A. 2008. Robust but delayed thalamocortical activation of dendritic-targeting inhibitory interneurons. *Proc Natl Acad Sci U S A.* 105:2187–2192.
- Thomson AM. 2010. Neocortical layer 6, a review. *Front Neuroanat.* 4:13.
- Tian MK, Bailey CD, Lambe EK. 2014. Cholinergic excitation in mouse primary vs. associative cortex: region-specific magnitude and receptor balance. *Eur J Neurosci.* 40:2608–2618.
- van Aerde KI, Feldmeyer D. 2015. Morphological and physiological characterization of pyramidal neuron subtypes in rat medial prefrontal cortex. *Cereb Cortex.* 25:788–805.
- Velez-Fort M, Rousseau CV, Niedworok CJ, Wickersham IR, Rancz EA, Brown APY, Strom M, Margrie TW. 2014. The stimulus selectivity and connectivity of layer six principal cells reveals cortical microcircuits underlying visual processing. *Neuron.* 84:238.
- Wang Q, Ng L, Harris JA, Feng D, Li Y, Royall JJ, Oh SW, Bernard A, Sunkin SM, Koch C, et al. 2017. Organization of the connections between claustrum and cortex in the mouse. *J Comp Neurol.* 525:1317–1346.
- Ward JH. 1963. Hierarchical grouping to optimize an objective function. *J Am Stat Assoc.* 58:236–244.
- West DC, Mercer A, Kirchhecker S, Morris OT, Thomson AM. 2006. Layer 6 cortico-thalamic pyramidal cells preferentially innervate interneurons and generate facilitating EPSPs. *Cereb Cortex.* 16:200–211.
- White MG, Mathur BN. 2018. Frontal cortical control of posterior sensory and association cortices through the claustrum. *Brain Struct Funct.* 223:2999–3006.
- Whitesell JD, Liska A, Coletta L, Hirokawa KE, Bohn P, Williford A, Groblewski PA, Graddis N, Kuan L, Knox JE, et al. 2020. Regional, layer, and cell-type-specific connectivity of the mouse default mode network. *Neuron.* 109:545–559.
- Woo TU, Beale JM, Finlay BL. 1991. Dual fate of subplate neurons in a rodent. *Cereb Cortex.* 1:433–443.
- Yang D, Gunter R, Qi G, Radnikow G, Feldmeyer D. 2020. Muscarinic and nicotinic modulation of neocortical layer 6A synaptic microcircuits is cooperative and cell-specific. *Cereb Cortex.* 30:3528–3542.
- Yuste R, Hawrylycz M, Aalling N, Aguilar-Valles A, Arendt D, Arnedillo RA, Ascoli GA, Bielza C, Bokharaie V, Bergmann TB, et al. 2020. A community-based transcriptomics classification and nomenclature of neocortical cell types. *Nat Neurosci.* 23:1456–1468.
- Zakiewicz IM, Bjaalie JG, Leergaard TB. 2014. Brain-wide map of efferent projections from rat barrel cortex. *Front Neuroinform.* 8:5.
- Zhang ZW, Deschenes M. 1997. Intracortical axonal projections of lamina VI cells of the primary somatosensory cortex in the rat: a single-cell labeling study. *J Neurosci.* 17:6365–6379.
- Zhang ZW, Deschenes M. 1998. Projections to layer VI of the posteromedial barrel field in the rat: a reappraisal of the role of corticothalamic pathways. *Cereb Cortex.* 8:428–436.
- Ziegler DA, Pritchett DL, Hosseini-Varnamkhasti P, Corkin S, Hamalainen M, Moore CI, Jones SR. 2010. Transformations in oscillatory activity and evoked responses in primary somatosensory cortex in middle age: a combined computational neural modeling and MEG study. *Neuroimage.* 52:897–912.
- Zingg B, Dong HW, Tao HW, Zhang LI. 2018. Input-output organization of the mouse claustrum. *J Comp Neurol.* 526:2428–2443.